Search for gravitational waves associated with 39 gamma-ray bursts using data from the second, third, and fourth LIGO runs

B. Abbott,[15] R. Abbott,[15] R. Adhikari,[15] J. Agresti,[15] P. Ajith,[2] B. Allen,[2,54] R. Amin,[19] S. B. Anderson,[15] W. G. Anderson,[54] M. Arain,[41] M. Araya,[15] H. Armandula,[15] M. Ashley,[4] S. Aston,[40] P. Aufmuth,[38] C. Aulbert,[1] S. Babak,[1] S. Ballmer,[15] H. Bantilan,[9] B. C. Barish,[15] C. Barker,[16] D. Barker,[16] B. Barr,[42] P. Barriga,[53] M. A. Barton,[42] K. Bayer,[18] K. Belczynski,[26] S. J. Berukoff,[1] J. Betzwieser,[18] P. T. Beyersdorf,[29] B. Bhawal,[15] I. A. Bilenko,[23] G. Billingsley,[15] R. Biswas,[54] E. Black,[15] K. Blackburn,[15] L. Blackburn,[18] D. Blair,[53] B. Bland,[16] J. Bogenstahl,[42] L. Bogue,[17] R. Bork,[15] V. Boschi,[15] S. Bose,[56] P. R. Brady,[54] V. B. Braginsky,[23] J. E. Brau,[45] M. Brinkmann,[2] A. Brooks,[39] D. A. Brown,[15,7] A. Bullington,[32] A. Bunkowski,[2] A. Buonanno,[43] O. Burmeister,[2] D. Busby,[15] W. E. Butler,[46] R. L. Byer,[32] L. Cadonati,[18] G. Cagnoli,[42] J. B. Camp,[24] J. Cannizzo,[24] K. Cannon,[54] C. A. Cantley,[42] J. Cao,[18] L. Cardenas,[15] K. Carter,[17] M. M. Casey,[42] G. Castaldi,[48] C. Cepeda,[15] E. Chalkley,[42] P. Charlton,[10] S. Chatterji,[15] S. Chelkowski,[2] Y. Chen,[1] F. Chiadini,[47] D. Chin,[44] E. Chin,[53] J. Chow,[4] N. Christensen,[9] J. Clark,[42] P. Cochrane,[2] T. Cokelaer,[8] C. N. Colacino,[40] R. Coldwell,[41] M. Coles,[17] R. Conte,[47] D. Cook,[16] T. Corbitt,[18] D. Coward,[53] D. Coyne,[15] J. D. E. Creighton,[54] T. D. Creighton,[15] R. P. Croce,[48] D. R. M. Crooks,[42] A. M. Cruise,[40] P. Csatorday,[18] A. Cumming,[42] J. Dalrymple,[33] E. D'Ambrosio,[15] K. Danzmann,[38,2] G. Davies,[8] E. Daw,[49] D. DeBra,[32] J. Degallaix,[53] M. Degree,[32] T. Delker,[41] T. Demma,[48] V. Dergachev,[44] S. Desai,[34] R. DeSalvo,[15] S. Dhurandhar,[14] M. Díaz,[35] J. Dickson,[4] A. Di Credico,[33] G. Diederichs,[38] A. Dietz,[8] H. Ding,[15] E. E. Doomes,[31] R. W. P. Drever,[5] J.-C. Dumas,[53] R. J. Dupuis,[15] J. G. Dwyer,[11] P. Ehrens,[15] E. Espinoza,[15] T. Etzel,[15] M. Evans,[15] T. Evans,[17] S. Fairhurst,[8,15] Y. Fan,[53] D. Fazi,[15] M. M. Fejer,[32] L. S. Finn,[34] V. Fiumara,[47] N. Fotopoulos,[54] A. Franzen,[38] K. Y. Franzen,[41] A. Freise,[40] R. Frey,[45] T. Fricke,[46] P. Fritschel,[18] V. V. Frolov,[17] M. Fyffe,[17] V. Galdi,[48] K. S. Ganezer,[6] J. Garofoli,[16] I. Gholami,[1] J. A. Giaime,[17,19] S. Giampanis,[46] K. D. Giardina,[17] K. Goda,[18] E. Goetz,[44] L. Goggin,[15] G. González,[19] S. Gossler,[4] A. Grant,[42] S. Gras,[53] C. Gray,[16] M. Gray,[4] J. Greenhalgh,[28] A. M. Gretarsson,[12] R. Grosso,[35] H. Grote,[2] S. Grunewald,[1] M. Guenther,[16] R. Gustafson,[44] B. Hage,[38] D. Hammer,[54] C. Hanna,[19] J. Hanson,[17] J. Harms,[2] G. Harry,[18] E. Harstad,[45] T. Hayler,[28] J. Heefner,[15] G. Heinzel,[2] I. S. Heng,[42] A. Heptonstall,[42] M. Heurs,[2] M. Hewitson,[2] S. Hild,[38] E. Hirose,[33] D. Hoak,[17] D. Hosken,[39] J. Hough,[42] E. Howell,[53] D. Hoyland,[40] S. H. Huttner,[42] D. Ingram,[16] E. Innerhofer,[18] M. Ito,[45] Y. Itoh,[54] A. Ivanov,[15] D. Jackrel,[32] O. Jennrich,[42] B. Johnson,[16] W. W. Johnson,[19] W. R. Johnston,[35] D. I. Jones,[50] G. Jones,[8] R. Jones,[42] L. Ju,[53] P. Kalmus,[11] V. Kalogera,[26] D. Kasprzyk,[40] E. Katsavounidis,[18] K. Kawabe,[16] S. Kawamura,[25] F. Kawazoe,[25] W. Kells,[15] D. G. Keppel,[15] F. Ya. Khalili,[23] C. J. Killow,[42] C. Kim,[26] P. King,[15] J. S. Kissel,[19] S. Klimenko,[41] K. Kokeyama,[25] V. Kondrashov,[15] R. K. Kopparapu,[19] D. Kozak,[15] B. Krishnan,[1] P. Kwee,[38] P. K. Lam,[4] M. Landry,[16] B. Lantz,[32] A. Lazzarini,[15] B. Lee,[53] M. Lei,[15] J. Leiner,[56] V. Leonhardt,[25] I. Leonor,[45] K. Libbrecht,[15] A. Libson,[9] P. Lindquist,[15] N. A. Lockerbie,[51] J. Logan,[15] M. Longo,[47] M. Lormand,[17] M. Lubinski,[16] H. Lück,[38,2] B. Machenschalk,[1] M. MacInnis,[18] M. Mageswaran,[15] K. Mailand,[15] M. Malec,[38] V. Mandic,[15] S. Marano,[47] S. Márka,[11] J. Markowitz,[18] E. Maros,[15] I. Martin,[42] J. N. Marx,[15] K. Mason,[18] L. Matone,[11] V. Matta,[47] N. Mavalvala,[18] R. McCarthy,[16] D. E. McClelland,[4] S. C. McGuire,[31] M. McHugh,[21] K. McKenzie,[4] J. W. C. McNabb,[34] S. McWilliams,[24] T. Meier,[38] A. Melissinos,[46] G. Mendell,[16] R. A. Mercer,[41] S. Meshkov,[15] E. Messaritaki,[15] C. J. Messenger,[42] D. Meyers,[15] E. Mikhailov,[18] S. Mitra,[14] V. P. Mitrofanov,[23] G. Mitselmakher,[41] R. Mittleman,[18] O. Miyakawa,[15] S. Mohanty,[35] G. Moreno,[16] K. Mossavi,[2] C. MowLowry,[4] A. Moylan,[4] D. Mudge,[39] G. Mueller,[41] S. Mukherjee,[35] H. Müller-Ebhardt,[2] J. Munch,[39] P. Murray,[42] E. Myers,[16] J. Myers,[16] S. Nagano,[2] T. Nash,[15] G. Newton,[42] A. Nishizawa,[25] F. Nocera,[15] K. Numata,[24] P. Nutzman,[26] B. O'Reilly,[17] R. O'Shaughnessy,[26] D. J. Ottaway,[18] H. Overmier,[17] B. J. Owen,[34] Y. Pan,[43] M. A. Papa,[1,54] V. Parameshwaraiah,[16] C. Parameswariah,[17] P. Patel,[15] M. Pedraza,[15] S. Penn,[13] V. Pierro,[48] I. M. Pinto,[48] M. Pitkin,[42] H. Pletsch,[2] M. V. Plissi,[42] F. Postiglione,[47] R. Prix,[1] V. Quetschke,[41] F. Raab,[16] D. Rabeling,[4] H. Radkins,[16] R. Rahkola,[45] N. Rainer,[2] M. Rakhmanov,[34] M. Ramsunder,[34] K. Rawlins,[18] S. Ray-Majumder,[54] V. Re,[40] T. Regimbau,[8] H. Rehbein,[2] S. Reid,[42] D. H. Reitze,[41] L. Ribichini,[2] S. Richman,[18] R. Riesen,[17] K. Riles,[44] B. Rivera,[16] N. A. Robertson,[15,42] C. Robinson,[8] E. L. Robinson,[40] S. Roddy,[17] A. Rodriguez,[19] A. M. Rogan,[56] J. Rollins,[11] J. D. Romano,[8] J. Romie,[17] H. Rong,[41] R. Route,[32] S. Rowan,[42] A. Rüdiger,[2] L. Ruet,[18] P. Russell,[15] K. Ryan,[16] S. Sakata,[25] M. Samidi,[15] L. Sancho de la Jordana,[37] V. Sandberg,[16] G. H. Sanders,[15] V. Sannibale,[15] S. Saraf,[27] P. Sarin,[18] B. S. Sathyaprakash,[8] S. Sato,[25] P. R. Saulson,[33] R. Savage,[16] P. Savov,[7] A. Sazonov,[41] S. Schediwy,[53] R. Schilling,[2] R. Schnabel,[2] R. Schofield,[45] B. F. Schutz,[1] P. Schwinberg,[16] S. M. Scott,[4] A. C. Searle,[4] B. Sears,[15] F. Seifert,[2] D. Sellers,[17] A. S. Sengupta,[8] P. Shawhan,[43] D. H. Shoemaker,[18] A. Sibley,[17] J. A. Sidles,[52] X. Siemens,[15,7] D. Sigg,[16] S. Sinha,[32] A. M. Sintes,[37,1] B. J. J. Slagmolen,[4] J. Slutsky,[19] J. R. Smith,[2] M. R. Smith,[15] K. Somiya,[2,1] K. A. Strain,[42]

 © 2008 The American Physical Society

N. E. Strand,[34] D. M. Strom,[45] A. Stuver,[34] T. Z. Summerscales,[3] K.-X. Sun,[32] M. Sung,[19] P. J. Sutton,[15] J. Sylvestre,[15] H. Takahashi,[1] A. Takamori,[15] D. B. Tanner,[41] M. Tarallo,[15] R. Taylor,[15] R. Taylor,[42] J. Thacker,[17] K. A. Thorne,[34] K. S. Thorne,[7] A. Thüring,[38] M. Tinto,[5] K. V. Tokmakov,[42] C. Torres,[35] C. Torrie,[42] G. Traylor,[17] M. Trias,[37] W. Tyler,[15] D. Ugolini,[36] C. Ungarelli,[40] K. Urbanek,[32] H. Vahlbruch,[38] M. Vallisneri,[7] C. Van Den Broeck,[8] M. van Putten,[18] M. Varvella,[15] S. Vass,[15] A. Vecchio,[40] J. Veitch,[42] P. Veitch,[39] A. Villar,[15] C. Vorvick,[16] S. P. Vyachanin,[23] S. J. Waldman,[15] L. Wallace,[15] H. Ward,[42] R. Ward,[15] K. Watts,[17] D. Webber,[15] A. Weidner,[2] M. Weinert,[2] A. Weinstein,[15] R. Weiss,[18] L. Wen,[1] S. Wen,[19] K. Wette,[4] J. T. Whelan,[1] D. M. Whitbeck,[34] S. E. Whitcomb,[15] B. F. Whiting,[41] S. Wiley,[6] C. Wilkinson,[16] P. A. Willems,[15] L. Williams,[41] B. Willke,[38,2] I. Wilmut,[28] W. Winkler,[2] C. C. Wipf,[18] S. Wise,[41] A. G. Wiseman,[54] G. Woan,[42] D. Woods,[54] R. Wooley,[17] J. Worden,[16] W. Wu,[41] I. Yakushin,[17] H. Yamamoto,[15] Z. Yan,[53] S. Yoshida,[30] N. Yunes,[34] K. D. Zaleski,[34] M. Zanolin,[18] J. Zhang,[44] L. Zhang,[15] C. Zhao,[53] N. Zotov,[20] M. Zucker,[18] H. zur Mühlen,[38] and J. Zweizig[15]

(The LIGO Scientific Collaboration)*

[1]*Albert-Einstein-Institut, Max-Planck-Institut für Gravitationsphysik, D-14476 Golm, Germany*
[2]*Albert-Einstein-Institut, Max-Planck-Institut für Gravitationsphysik, D-30167 Hannover, Germany*
[3]*Andrews University, Berrien Springs, Michigan 49104 USA*
[4]*Australian National University, Canberra, 0200, Australia*
[5]*California Institute of Technology, Pasadena, California 91125, USA*
[6]*California State University Dominguez Hills, Carson, California 90747, USA*
[7]*Caltech–CaRT, Pasadena, California 91125, USA*
[8]*Cardiff University, Cardiff, CF24 3AA, United Kingdom*
[9]*Carleton College, Northfield, Minnesota 55057, USA*
[10]*Charles Sturt University, Wagga Wagga, NSW 2678, Australia*
[11]*Columbia University, New York, New York 10027, USA*
[12]*Embry-Riddle Aeronautical University, Prescott, Arizona 86301 USA*
[13]*Hobart and William Smith Colleges, Geneva, New York 14456, USA*
[14]*Inter-University Centre for Astronomy and Astrophysics, Pune - 411007, India*
[15]*LIGO–California Institute of Technology, Pasadena, California 91125, USA*
[16]*LIGO Hanford Observatory, Richland, Washington 99352, USA*
[17]*LIGO Livingston Observatory, Livingston, Louisiana 70754, USA*
[18]*LIGO–Massachusetts Institute of Technology, Cambridge, Massachusetts 02139, USA*
[19]*Louisiana State University, Baton Rouge, Louisiana 70803, USA*
[20]*Louisiana Tech University, Ruston, Louisiana 71272, USA*
[21]*Loyola University, New Orleans, Louisiana 70118, USA*
[22]*Max Planck Institut für Quantenoptik, D-85748, Garching, Germany*
[23]*Moscow State University, Moscow, 119992, Russia*
[24]*NASA/Goddard Space Flight Center, Greenbelt, Maryland 20771, USA*
[25]*National Astronomical Observatory of Japan, Tokyo 181-8588, Japan*
[26]*Northwestern University, Evanston, Illinois 60208, USA*
[27]*Rochester Institute of Technology, Rochester, New York 14623, USA*
[28]*Rutherford Appleton Laboratory, Chilton, Didcot, Oxon OX11 0QX United Kingdom*
[29]*San Jose State University, San Jose, California 95192, USA*
[30]*Southeastern Louisiana University, Hammond, Louisiana 70402, USA*
[31]*Southern University and A&M College, Baton Rouge, Louisiana 70813, USA*
[32]*Stanford University, Stanford, California 94305, USA*
[33]*Syracuse University, Syracuse, New York 13244, USA*
[34]*The Pennsylvania State University, University Park, Pennsylvania 16802, USA*
[35]*The University of Texas at Brownsville and Texas Southmost College, Brownsville, Texas 78520, USA*
[36]*Trinity University, San Antonio, Texas 78212, USA*
[37]*Universitat de les Illes Balears, E-07122 Palma de Mallorca, Spain*
[38]*Universität Hannover, D-30167 Hannover, Germany*
[39]*University of Adelaide, Adelaide, SA 5005, Australia*
[40]*University of Birmingham, Birmingham, B15 2TT, United Kingdom*
[41]*University of Florida, Gainesville, Florida 32611, USA*
[42]*University of Glasgow, Glasgow, G12 8QQ, United Kingdom*
[43]*University of Maryland, College Park, Maryland 20742 USA*
[44]*University of Michigan, Ann Arbor, Michigan 48109, USA*

[45]University of Oregon, Eugene, Oregon 97403, USA
[46]University of Rochester, Rochester, New York 14627, USA
[47]University of Salerno, 84084 Fisciano (Salerno), Italy
[48]University of Sannio at Benevento, I-82100 Benevento, Italy
[49]University of Sheffield, Sheffield, S3 7RH, United Kingdom
[50]University of Southampton, Southampton, SO17 1BJ, United Kingdom
[51]University of Strathclyde, Glasgow, G1 1XQ, United Kingdom
[52]University of Washington, Seattle, Washington, 98195, USA
[53]University of Western Australia, Crawley, WA 6009, Australia
[54]University of Wisconsin-Milwaukee, Milwaukee, Wisconsin 53201, USA
[55]Vassar College, Poughkeepsie, New York 12604, USA
[56]Washington State University, Pullman, Washington 99164, USA
(Received 16 October 2007; published 17 March 2008)

We present the results of a search for short-duration gravitational-wave bursts associated with 39 gamma-ray bursts (GRBs) detected by gamma-ray satellite experiments during LIGO's S2, S3, and S4 science runs. The search involves calculating the crosscorrelation between two interferometer data streams surrounding the GRB trigger time. We search for associated gravitational radiation from single GRBs, and also apply statistical tests to search for a gravitational-wave signature associated with the whole sample. For the sample examined, we find no evidence for the association of gravitational radiation with GRBs, either on a single-GRB basis or on a statistical basis. Simulating gravitational-wave bursts with sine-Gaussian waveforms, we set upper limits on the root-sum-square of the gravitational-wave strain amplitude of such waveforms at the times of the GRB triggers. We also demonstrate how a sample of several GRBs can be used collectively to set constraints on population models. The small number of GRBs and the significant change in sensitivity of the detectors over the three runs, however, limits the usefulness of a population study for the S2, S3, and S4 runs. Finally, we discuss prospects for the search sensitivity for the ongoing S5 run, and beyond for the next generation of detectors.

DOI: 10.1103/PhysRevD.77.062004 PACS numbers: 04.80.Nn, 04.30.Tv, 95.85.Sz

I. INTRODUCTION

It has been over three decades since gamma-ray bursts (GRBs) were first detected by the *Vela* satellites [1]. During the 1990s, when the *Burst and Transient Source Experiment* (BATSE) [2] and BeppoSAX [3] were in operation, important discoveries and observations relating to GRBs were made, such as the isotropic distribution of GRBs [4]; the bimodal distribution of burst durations, suggesting long and short classes of GRBs [5]; detections of the first x-ray [6], optical [7], and radio [8] counterparts; the first redshift measurements [9–11]; and the first hints of the association of long-duration GRBs with core-collapse supernovae [12–14]. Today, important questions about GRB progenitors, emission mechanisms, and geometry linger, and observations made by the current generation of gamma-ray satellite experiments such as Swift [15], HETE-2 [16], INTEGRAL [17], and others continue to provide new and exciting information which help us answer these questions and better understand the origin and physics of these astrophysical objects.

Currently favored models of GRB progenitors are core-collapse supernovae for long-duration GRBs [18], and neutron star-neutron star (NS-NS) or neutron star-black hole (NS-BH) mergers for short-duration GRBs [19,20]. These models and the division into two classes of progenitors are supported by observations of supernovae associated with long-duration GRBs [12–14,21,22] and, more recently, observations of afterglows and identification of host galaxies for short-duration GRBs [23–26]. The end result in either scenario is the formation of a stellar-mass black hole [27] and, in either scenario, theory predicts the emission of gravitational radiation. In the former case, gravitational waves would result from the collapse of a massive star's core, while in the latter case, gravitational radiation would result from the inspiral, merger, and ring-down phases of the coalescence. Recently, there has been an observation-driven suggestion of a third class of GRBs which could include both short- and long-duration GRBs [28], but more observations are needed to support this suggestion.

Because of the expected evolution of the proposed progenitors, the redshift distribution of long-duration GRBs is thought to follow the star formation rate of the Universe [29,30], and recent redshift measurements tend to support this model, with the measured GRB redshift distribution peaking at $z \gtrsim 1$ [31]. Long-duration GRBs have also been associated exclusively with late-type star-forming host galaxies [32]. On the other hand, the recent observations of x-ray and optical afterglows from a few short-duration bursts seem to suggest that these GRBs are located at lower redshifts relative to long-duration GRBs [25,33], and that short bursts are found in a mixture of galaxy types, including elliptical galaxies, which have older stellar populations. All of these observations are consistent with the currently favored models of GRB progenitors. Although

*http://www.ligo.org

a large fraction of GRBs are too distant for any associated gravitational-wave (GW) signals to be detected by LIGO, it is plausible that a small fraction occur at closer distances. For example, a redshift of $z = 0.0085$, or a distance of 35 Mpc, has been associated with long-duration burst/supernova GRB 980425/SN 1998bw [12]. It is not unreasonable to expect that a few GRBs with no measured redshifts could have been located relatively nearby as well. For short-duration GRBs, the recent redshift observations have led to fairly optimistic estimates [34,35] for an associated GW observation in an extended LIGO science run.

In this paper, we present the results of a search for short-duration gravitational-wave bursts (GWBs) associated with 39 GRBs that were detected by gamma-ray satellite experiments on dates when the S2, S3, and S4 science runs of the Laser Interferometer Gravitational-Wave Observatory (LIGO) were in progress. Although the theoretical shapes of the GW burst signals resulting from the two progenitor scenarios are not known, many models predict that the GW signals would be of short duration, ranging from $\sim$1 ms to $\sim$100 ms [36–40]. The search method presented here targets such short-duration signals and calculates the crosscorrelation between two LIGO interferometer data streams to look for these signals. A crosscorrelation-based method efficiently suppresses uncorrelated transient noise in the data streams, and at the same time tests that a candidate GW signal appears in data from at least two interferometers [41]. Previously, we presented the results of a search for a GWB associated with the bright and nearby GRB 030329 [42]. Here, we present analysis methods which search for GWBs associated with GRBs not only on an individual-GRB basis to target loud GWBs, but also on a statistical basis. The statistical approach is sensitive to the cumulative effect of any weak GW signals that may be present in the LIGO data.

It is noted here that for the compact binary coalescence models of short-duration GRBs, a subset of the associated inspiral waveforms are well modeled, and that a template-based search for inspiral GW signals associated with short-duration GRBs is currently being developed using LIGO data.

II. LIGO S2, S3, AND S4 SCIENCE RUNS

The LIGO interferometers (IFOs) have been described in detail elsewhere [43]. These detectors are kilometer-length Michelson interferometers with orthogonal Fabry-Perot arms, designed to detect impinging gravitational waves with frequencies ranging from $\sim$40 Hz to several kilohertz. The interferometers' maximum sensitivity occurs near 100 Hz to 200 Hz. There are two LIGO observatories: one located at Hanford, WA (LHO) and the other at Livingston, LA (LLO). There are two IFOs at LHO: one IFO with 4-km arms (H1) and the other with 2-km arms (H2). The LLO observatory has one 4-km IFO (L1). The observatories are separated by a distance of 3000 km, corresponding to a time-of-flight separation of 10 ms.

Each IFO consists of mirrors at the ends of each arm which serve as test masses. Data from each IFO is in the form of a time series, digitized at 16 384 samples/s, which records the differential length of the arms and which, when calibrated, measures the strain induced by a gravitational wave. The response of an IFO to a given strain is measured by injecting sinusoidal excitations with known amplitude into the test mass control systems and tracking the resulting signals at the measurement point throughout each run. The result is a measurement of the time-varying, frequency-dependent response function of each IFO.

The LIGO S2 run was held from February to April 2003 (59 days), the S3 run from October 2003 to January 2004 (70 days), and the S4 run from February to March 2005 (29 days). The sensitivity of the LIGO detectors improved significantly between the S2 and S4 runs, and approached the initial LIGO design sensitivity during the LIGO S4 run. The progression of the best LIGO sensitivity from the S2 to S4 runs is shown in Fig. 1. For each run, the corresponding curve in this plot gives the magnitude of the noise spectral density, in strain-equivalent units, for one of the IFOs during a representative time interval within the run. The solid curve gives the initial LIGO design sensitivity goal as given in LIGO's Science Requirements Document. Further, the duty factor of the three IFOs increased significantly from the S2 to S4 run. During the S2 run, the duty factors were 74%, 58%, and 37% for the H1, H2, and L1

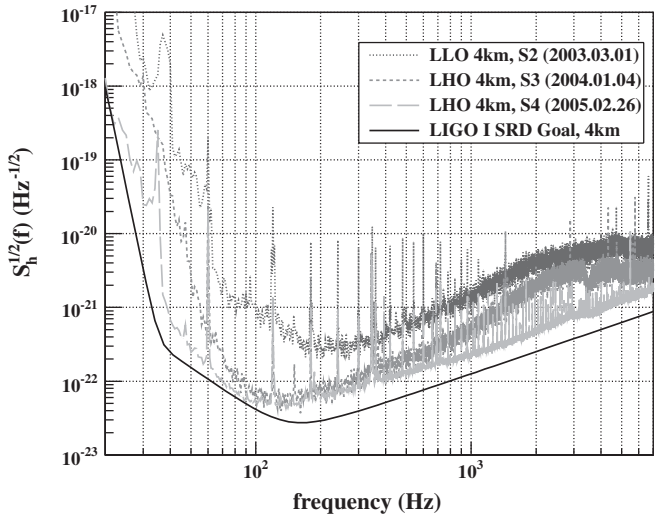

FIG. 1. Progression of LIGO sensitivities from S2 to S4 science runs. For each run, the corresponding curve gives the magnitude of the noise spectral density, in strain-equivalent units, for one of the IFOs during a representative time interval within the run. The solid curve gives the initial LIGO design sensitivity goal as given in LIGO's Science Requirements Document (SRD).

IFOs, respectively, while during the S4 run, the duty factors were 80.5%, 81.4%, and 74.5%, respectively.

III. THE GRB SAMPLE

Compared to the 1990s, when BATSE was detecting GRBs, the period from 2001 to 2004, when LIGO had its first three science runs, was a time of relatively low GRB detection rate. LIGO's S4 run coincided with a time when Swift had just started operating and was making its first GRB detections. There were 29 GRB triggers during the S2 run, 11 GRB triggers during S3, and 6 GRB triggers during S4. These GRB triggers were provided by the Third Interplanetary Network (IPN) [44], Konus-Wind [45], HETE-2, INTEGRAL, and Swift, and were distributed via the GRB Coordinates Network (GCN) [46].

Only LIGO data which were of science mode quality were analyzed. These science mode segments are data collected when the interferometers were in a stable, resonant configuration. Additionally, data segments which were flagged as being of poor quality were not included in the analysis. For example, data segments which were known to have a high rate of seismic transients were excluded from the analysis. After all the data quality cuts were made, there were 28 GRBs left to be analyzed for the S2 run, 7 GRBs for S3, and 4 GRBs for S4, for a total of 39 GRB triggers. Of these, 22 GRBs had positions well-localized to within a few arcminutes, while 17 GRBs did not. These 17 GRBs were detected by either HETE or IPN. In the case of HETE, no position measurements were available while, in the case of IPN, the GRBs were not well-localized. Of the 39 GRBs, six had redshift measurements, four of which were at $z > 1$, and two fell in the short-duration category of bursts, i.e. had durations ≤ 2 seconds. For this analysis, due to the small size of the sample, we did not attempt to differentiate the GRBs according to their observed properties. The use of a classification scheme in a search can be done in the future with a larger GRB sample.

Information about most of the GRBs was collected from the corresponding GCN circulars. The parameters that are relevant for this analysis are the GRB date and trigger time, and the right ascension and declination. For those HETE GRBs which did not have positions, information about the GRB trigger time was obtained from the HETE website [47]. A list of the GRBs analyzed and relevant information are given in Table I.

IV. DATA ANALYSIS

A. On-source and off-source data segments

Since GRBs have well-measured detection times, the search for short-duration GW signals can be limited to time segments—called *on-source* segments here—surrounding the GRB trigger times. Limiting the search to encompass only these time segments significantly reduces the number of search trials, compared to a search which makes use of data from the entire run. In case of a detection, such a reduction in trials translates to a larger significance for the detection compared to that which would result from an untriggered search.

Making use of on-source segments also means that background estimation can proceed by using data stretches—called *off-source* segments here—which are outside the on-source segments, but which are still close enough in time to the on-source segments so that the off-source data are similar in character to, and representative of, the on-source data.

In this analysis, the length of each on-source segment was chosen to be 180 seconds, with the first 120 seconds of the LIGO on-source data occurring before the GRB trigger time, and the last 60 seconds occurring after the trigger time. This window length is longer than the expected time delay between a gravitational-wave signal and the onset of a GRB signal, which is of the order of several seconds [48–50], but which in certain models can be as large as 100 seconds [51]. The large search window also takes into account the uncertainty in the definition of the measured GRB trigger time, i.e. it takes into account the possibility that the trigger time used in the analysis occurred before or after the actual start of a gamma-ray burst signal. Many gamma-ray light curves show subthreshold, precursor bursts which occur before the measured GRB trigger time, hence our choice of an asymmetric search window around the trigger time.

For each GRB, a search for a GW signal was carried out using data from each *pair* of IFOs that was operating properly at that time. Additionally, LHO-LLO on-source pairs were analyzed only when GRBs had well-defined positions, since position information is necessary to calculate the LHO-LLO time-of-flight delay. After all the data quality cuts were made, there were 59 IFO-IFO on-source pairs that were analyzed. This number is larger than the number of GRB triggers because, for each GRB trigger, it was possible to have up to three IFO pairs pass the data quality cuts. There were 35 H1-H2 on-source pairs analyzed, 12 for H1-L1, and 12 for H2-L1.

The software used in this analysis is available in the LIGO Scientific Collaboration's CVS archives with the tag multigrb_r1 in MATAPPS [52].

B. Data conditioning

Before the crosscorrelation between two LIGO data streams was calculated, the time-series data from each interferometer was conditioned. This consisted of whitening, phase-correction, and bandpassing from 40 Hz to 2000 Hz. The sampling rate was retained at 16 384 samples/s. Whitening was done to make sure the resulting spectrum of the data was flat instead of being dominated by low-frequency or high-frequency components. The procedure consisted of using one-second data units to whiten the

TABLE I. The GRB sample analyzed.

LIGO run	GRB[a] date	UTC[b] time	GPS[c] time	Duration[d] (seconds)	Right Ascension[e] (degrees)	Declination[f] (degrees)	F_{ave}[g] LHO	F_{ave}[g] LLO	Time delay[h] (seconds)	IFO[i]
S2	030215	17:11:52	729 364 325.00	40	...	...	...	...	...	H1, H2
	030215a	11:13:32	729 342 825.00	30	...	...	...	...	...	H1, H2
	030215b	11:16:28	729 343 001.00	40	...	...	...	...	...	H1, H2
	030216	16:13:44	729 447 237.00	3	...	...	...	...	...	H1, H2
	030217	02:45:42	729 485 155.00	50	186.596	−11.850	0.379	0.204	0.007 886 7	H2, L1
	030218	11:42:38	729 603 771.00	200	...	...	...	...	...	H1, H2
	030221	07:46:14	729 848 787.00	...	...	...	...	...	...	H1, H2
	030223	09:45:06	730 028 719.00	10	...	...	...	...	...	H1, H2
	030226[j]	03:46:31.99	730 266 404.99	22	173.254	25.900	0.356	0.524	0.005 989 2	H1, H2, L1
	030228	20:26:46	730 499 219.00	15	...	...	...	...	...	H1, H2
	030301	20:27:20	730 585 653.00	30	...	...	...	...	...	H1, H2
	030308	14:06:09	731 167 582.00	...	...	...	...	...	...	H1, H2
	030320a	10:11:40	732 190 313.00	80	267.929	−25.317	0.317	0.418	0.009 317 2	H1, H2, L1
	030320b	18:49:17	732 221 370.00	150	...	...	...	...	...	H1, H2
	030323a	08:42:24	732 444 157.00	5	297.250	−12.500	0.269	0.131	0.008 876 2	H1, H2, L1
	030323b[k]	21:56:57.60	732 491 830.60	25	166.525	−21.900	0.533	0.336	0.006 459 3	H1, H2, L1
	030324	03:12:42.80	732 510 775.80	45	204.296	−0.317	0.148	0.288	0.008 671 6	H1, H2
	030325	14:15:10	732 636 923.00	2	70.808	−19.133	0.592	0.480	0.003 966 0	H1, H2, L1
	030326	10:43:41	732 710 634.00	10	292.967	−11.717	0.191	0.407	0.009 425 7	H1, H2, L1
	030329	03:31:43	732 943 916.00	...	...	...	...	...	...	H1, H2
	030329a[l]	11:37:14.67	732 973 047.67	22.8	161.208	21.517	0.265	0.051	−0.009 509 0	H1, H2
	030329b	15:34:15.35	732 987 268.35	65	160.626	−48.572	0.635	0.665	−0.000 992 7	H1, H2
	030331	05:38:40.82	733 124 333.82	10	349.261	36.260	0.252	0.312	−0.005 753 9	H1, L1
	030405	02:17:28	733 544 261.00	5	248.275	−24.150	0.565	0.377	0.005 997 5	H1, H2, L1
	030406	22:42:07	733 704 140.00	65	285.429	−68.083	0.598	0.551	0.001 433 8	H1, L1
	030410	11:23:42	734 009 035.00	0.3	...	...	...	...	...	H1, H2
	030413	07:34:37	734 254 490.00	15	198.604	62.350	0.680	0.586	−0.003 185 8	H2, L1
	030414	13:48:27	734 363 320.00	40	119.887	−48.583	0.702	0.653	0.001 530 8	H1, H2
S3	031108	14:11:01	752 335 874.00	22	66.729	−5.930	0.278	0.313	−0.007 526 4	H1, H2
	031109a	11:11:48	752 411 521.00	59	327.765	20.203	0.336	0.464	−0.008 832 4	H1, H2
	031123	22:41:14	753 662 487.00	...	...	...	...	...	...	H1, H2
	031127a	18:58:58	753 994 751.00	10	...	...	...	...	...	H1, H2
	031127b	18:59:16	753 994 769.00	70	...	...	...	...	...	H1, H2
	031130	02:04:48	754 193 101.00	4	...	...	...	...	...	H1, H2
	031220	03:29:56.74	755 926 209.74	16.9	69.893	7.374	0.414	0.617	0.006 864 3	H1, H2
S4	050223[m]	03:09:06	793 163 359.00	23	271.390	−62.481	0.676	0.596	0.002 703 1	H1, H2
	050306	03:33:12	794 115 205.00	160	282.337	−9.162	0.565	0.610	−0.001 342 5	H1, H2, L1
	050318[n]	15:44:37	795 195 890.00	32	49.651	−46.392	0.528	0.293	0.008 307 5	H1, H2, L1
	050319[o]	09:31:18.44	795 259 891.44	10	154.202	43.546	0.597	0.370	−0.007 054 6	H1, H2, L1

[a]For GRBs with the same date, letters are appended to the date to distinguish the GRBs.
[b]UTC time of GRB trigger.
[c]GPS time of GRB trigger (seconds since 0h 6 Jan 1980 UTC).
[d]Duration of gamma-ray burst.
[e]Right ascension of GRB.
[f]Declination of GRB.
[g]Polarization-averaged antenna factor for specified IFO site [cf. Eq. (9)].
[h]Time-of-flight of GW signal between LHO and LLO. A positive value means that the signal arrived first at LLO; a negative value means that the signal arrived first at LHO.
[i]Interferometers which were analyzed.
[j]$z = 1.986$. [k]$z = 3.372$. [l]$z = 0.168$. [m]$z = 0.5915$. [n]$z = 1.44$. [o]$z = 3.24$.

adjacent one-second data and, as a consequence, removed any nonstationarity in the data having a time scale larger than 1 s. The whitening procedure also removed known lines.

The response functions of the three LIGO interferometers to a given GW strain signal are not exactly the same. A GW signal impinging on the three interferometers will thus appear as having slightly different phases in the corresponding time-series data (even after correcting for the LHO-LLO time-of-flight delay). Phase correction of the time-series data was therefore done to remove the differences that can be attributed to the different response functions of the interferometers. The phase-correction process made use of the measured, time-dependent, response functions of the interferometers.

C. Measuring the crosscorrelation statistic

The search method consisted of a ''binned'' search in which the 180-second conditioned on-source time series for each IFO was divided into time intervals (or bins) and the crosscorrelation for each IFO-IFO time bin pair calculated. Crosscorrelation bins of lengths 25 ms and 100 ms were used to target short-duration GW signals with durations of $\sim$1 ms to $\sim$100 ms. These crosscorrelation lengths were found, through simulations, to provide sufficient coverage of the targeted short-duration GW signals. Using bins much shorter than 25 ms would considerably increase the trials in the search, and therefore decrease the significance of a candidate GW event, while using bins much longer than 100 ms would considerably diminish the crosscorrelation strength of signals in the two data streams due to the increased duration of noise. The crosscorrelation, cc, is defined as

$$cc = \frac{\sum_{i=1}^{m}[s_1(i) - \mu_1][s_2(i) - \mu_2]}{\sqrt{\sum_{j=1}^{m}[s_1(j) - \mu_1]^2}\sqrt{\sum_{k=1}^{m}[s_2(k) - \mu_2]^2}} \quad (1)$$

where s_1 and s_2 are the two time series to be correlated, μ_1 and μ_2 are the corresponding means, and m is the number of samples in the crosscorrelation, i.e. the crosscorrelation integration length multiplied by the sampling rate of 16 384 samples/s. The possible values of the normalized crosscorrelation range from -1 to $+1$.

The bins were overlapped by half a bin width to avoid inefficiency in detecting signals occurring near a bin boundary. The crosscorrelation value was calculated for each IFO-IFO bin pair and, for each crosscorrelation bin length used, the largest crosscorrelation value—in the case of an H1-H2 search—obtained within the 180-second search window was considered the most significant measurement for that search, for that crosscorrelation bin length, for that IFO pair. In the case of an H1-L1 or H2-L1 search, it was the largest *absolute* value of the crosscorrelations that was taken as the most significant measurement. This was done to take into account the possibility that signals at LHO and LLO could be anticorrelated depending on the gravitational wave's (unknown) polarization. In the sections that follow, a reference to the ''largest crosscorrelation,'' in the case of an LHO-LLO analysis, will always mean the largest absolute value of crosscorrelations.

For those GRBs which had well-defined positions, the position of the GRB in the sky at the time of the burst was used to calculate the GW signal's time-of-flight delay between the LHO and LLO observatories. Each LHO-LLO pair of 180-second on-source segments were shifted in time relative to each other by the corresponding time-of-flight amount before the crosscorrelations were calculated. For those GRBs which were not well-localized, only H1-H2 on-source pairs were analyzed. For these GRBs, the maximum uncertainty in the LHO-LLO time delay is ± 10 ms, which is of the same scale as the signal durations targeted by the analysis, and such a time offset between signals at the two interferometers would have a considerable effect on the measured crosscorrelation.

D. Post-trials distributions

To estimate the significance of the loudest event, i.e. the largest crosscorrelation, that was found in an on-source

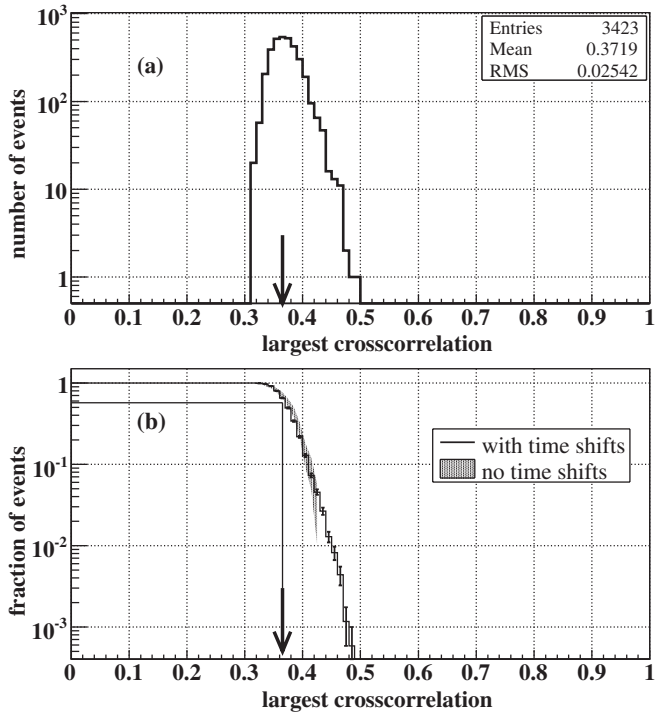

FIG. 2. (a) Example of a crosscorrelation post-trials distribution for the 25-ms crosscorrelation window, for the H1-H2 IFO pair. Data from off-source segments for GRB 050318 was used. (b) Cumulative distribution of (a), normalized to the total number of entries in the distribution. Both distributions with and without time shifts are shown, including the statistical errors. The arrow points to the largest crosscorrelation found in the on-source segment for GRB 050318. In this example, the largest crosscorrelation of 0.36 has a local probability of 0.57.

segment corresponding to a GRB and an IFO pair, we used off-source data within a few hours of the on-source data to measure the crosscorrelation distribution of the noise. This distribution was obtained for each GRB, for each IFO pair, for each crosscorrelation length by applying the search (described in Secs. IV B to IV C) on the off-source segments. The total length of the off-source region was about three hours surrounding the on-source segment. Each distribution was constructed by collecting the largest cross-correlation (or largest absolute value of crosscorrelations, in the case of H1-L1 and H2-L1) from each 180-second segment of the off-source region. This *post-trials* distribution takes into account the number of effective trials that was used in searching the on-source segment.

To obtain enough statistics for each distribution, time shifts were performed such that the time series of each IFO was shifted by multiples of 180 seconds relative to the other IFO and two 180-second stretches from the two IFOs were paired at each shift, making sure that two 180-second time stretches were paired only once for each distribution. The time shift procedure effectively increased the length of the off-source data to about 50 hours or more, typically.

As an example, the post-trials distribution for GRB 050318, for the H1-H2 IFO pair and for the 25-ms cross-correlation length, is shown in Fig. 2. For comparison, the cumulative plot shows both the distribution obtained with time shifts, and the distribution obtained without employing time shifts.

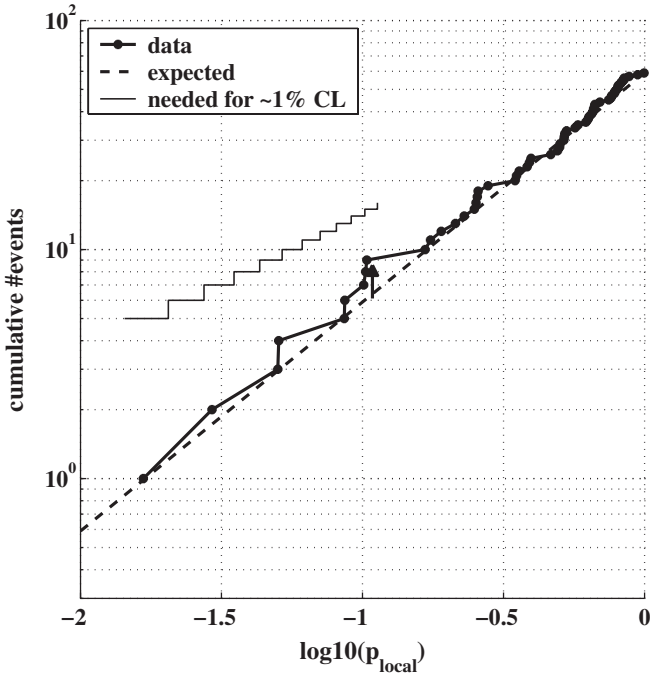

FIG. 3. Cumulative local probability distribution resulting from the search of 59 IFO-IFO on-source pairs using a 25-ms crosscorrelation length. The most significant excess is indicated by the arrow. The expected distribution under the null hypothesis is indicated by the bold, dashed line. The excess needed for a ~1% confidence in the null hypothesis is indicated by the solid line. The maximum excess indicated by this line is 15 events because only the 15 most significant events in the actual distribution are tested.

Each resulting post-trials distribution was used to estimate the cumulative probability that the largest crosscorrelation found in the corresponding on-source segment could be due to noise. This was done by determining what fraction of the distribution were at least as large as the loudest crosscorrelation found in the on-source segment. For example, the significance of the loudest 25-ms crosscorrelation found in the H1-H2 on-source segment of GRB 050318, indicated by an arrow in Fig. 2(b), can be estimated by using the plotted post-trials distribution. This probability will be referred to interchangeably in this paper as the post-trials, or *local*, probability of the on-source crosscorrelation statistic. This is also known in the literature as the *false alarm* probability.

Since H1 and H2 are colocated, environmental disturbances can give rise to correlated transient noise in the two interferometers. The effect of these correlated environmental noise on an H1-H2 crosscorrelation were, however, suppressed by: the judicious use of data quality cuts (cf. Sec. III), the applied data conditioning (cf. Sec. IV B), and the use of off-source data immediately surrounding the on-source data to estimate the background noise (cf. this section), which made it more likely that the background would properly reflect the rate of any correlated noise in the on-source data.

The cumulative distribution of local probabilities resulting from the search of 59 on-source segment pairs is shown

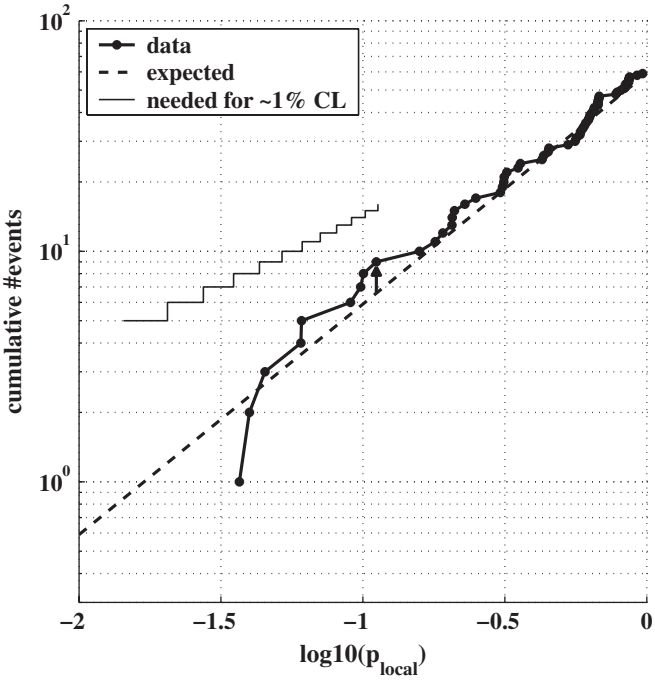

FIG. 4. Similar to Fig. 3, but using a 100-ms crosscorrelation length.

in Fig. 3 for the 25-ms crosscorrelation length, and in Fig. 4 for the 100-ms crosscorrelation length. Also shown (bold dashed lines) is the expected distribution under a null hypothesis. There were no loud events that were not consistent with the expected distribution, and we therefore conclude that there was no loud GW signal associated with any single GRB in the sample.

V. STATISTICAL TESTS

As mentioned earlier, GW signals from individual GRBs are likely to be weak in most cases due to the cosmological distances involved. Therefore, besides searching for GW signals from each GRB, we also consider the detection of a GW signature associated with a sample of several GRBs. Such approaches, first proposed in the context of GWs in [53], have already been used [54,55] to analyze resonant mass detector data using triggers from the BATSE and BeppoSAX missions.

We use two different statistical methods to look for a GW signature associated with a sample of multiple GRBs. As one may expect, the statistical performance of a method will depend on the nature of the underlying source population distribution. The two different methods presented here have complementary properties in this respect. The first statistical test presented, the binomial test, is most effective when several events contribute to the tail, i.e. the significant end, of the probability distribution of a sample. Moreover, it is also effective when there is a single significant event in the sample. The second test, the rank-sum test, is more effective at detecting the cumulative effect of weaker signals, but it is not very effective at detecting a few large events which fall on the tail of a probability distribution.

Since the signal strengths targeted by these two methods are slightly different, the resulting significances from the two methods can be different when there are real signals present in the sample. If a detection is claimed and the more significant measurement from the two statistical tests is chosen, then the proper statistical treatment, in order to arrive at a final significance, would be to impose a penalty factor for using two statistical tests to search for the cumulative signal.

A. Testing a probability distribution: The binomial test

Under a null hypothesis, the distribution of local probabilities is expected to be uniformly distributed from 0 to 1. The measured distribution of local probabilities was tested to search for an excess which may have been due to the cumulative effect of weak GW signals. In particular, we searched the tail of the distribution, or the smallest probabilities found in the on-source searches, by using the *binomial test*. To test the tail of a probability distribution, one first makes a choice as to how many events, n, in the tail would be tested out of the total number of events, N, in the sample. In this analysis, there were 59 IFO-IFO on-source pairs, and the upper 25% of the resulting probability sample, or the 15 most significant events, was tested. The probabilities of these n events are then sorted according to increasing value, i.e. decreasing significance: $p_1, p_2, p_3, \ldots, p_i, \ldots, p_n$. For each of these probabilities, p_i, one calculates the cumulative binomial probability, which is the probability for getting i or more events at least as significant as p_i:

$$P_{\geq i}(p_i) = P_i(p_i) + P_{i+1}(p_i) + P_{i+2}(p_i) + \ldots + P_N(p_i) \tag{2}$$

$$= 1 - [P_0(p_i) + P_1(p_i) + P_2(p_i) + \ldots + P_{i-1}(p_i)] \tag{3}$$

and where $P_i(p)$ is the binomial probability for getting i successes in N trials:

$$P_i(p) = \frac{N!}{i!(N-i)!} p^i (1-p)^{N-i}. \tag{4}$$

Here, N is the number of on-source searches, which is 59, and "success" means getting i events at least as significant as p. Note that if there is one loud event in the sample, with $p \ll 1$, then it follows from Eqs. (3) and (4) that the cumulative binomial probability is

$$P_{\geq 1}(p) = 1 - (1-p)^N \tag{5}$$

$$\approx Np. \tag{6}$$

Thus, the binomial test is able to automatically handle the case of a single loud event in the distribution.

After the cumulative binomial probability, $P_{\geq i}(p_i)$, has been calculated for each post-trials probability, p_i, the smallest binomial probability in the set is identified. This smallest binomial probability will point to the most significant excess that was found in searching the tail of the probability distribution.

The most significant excess that was found by the binomial test in the tail of the distribution is indicated by an arrow in Figs. 3 and 4. For the 25-ms distribution, the smallest binomial probability found was $P_{\geq 9}(p_9 = 0.104) = 0.153$. This means that the binomial test found that the most significant excess in the tail of the distribution consisted of nine events with local probabilities $p \leq 0.104$, and that the binomial probability for having nine or more events at least as significant as 0.104, given 59 trials, is 0.153.

In the case of the 100-ms distribution, the smallest binomial probability found was $P_{\geq 9}(p_9 = 0.112) = 0.207$. This means that the binomial test found that the most significant excess in the tail of the distribution consisted of nine events with local probabilities $p \leq 0.112$, and that the binomial probability for having nine or more events at least as significant as 0.112, given 59 trials, is 0.207.

Searching the tail of a post-trials probability distribution for the most significant excess introduces additional trials to the search. We thus need to test the most significant excess found in the tail of each local probability distribution against the null hypothesis to properly establish its level of significance. The expected distribution of the binomial probability statistic under the null hypothesis was obtained through simulations. The simulations consisted of randomly generating 59 numbers uniformly distributed from 0 to 1 to simulate 59 post-trials probabilities under the null hypothesis. Then the same binomial test that was applied to the actual post-trials probability distribution was applied to this distribution of random events to search for the most significant excess in the 15 most significant events in the tail. This was repeated 1×10^6 times, and the binomial probability of the most significant excess found in each trial was collected. The resulting distribution of binomial probabilities under the null hypothesis, in effect, takes into account the number of trials used in searching the tail of the post-trials distribution.

Results of these simulations show that, under the null hypothesis, the probability for getting a measurement at least as significant as 0.153 that was found in the 25-ms search is 0.48. In other words, under the null hypothesis, 1 in 2.1 sets of 59 on-source searches will result in a most significant excess with a binomial probability at least as significant as 0.153. This quantifies the conclusion that the result of the 25-ms search is consistent with the null hypothesis.

Similarly, we find that, under the null hypothesis, the probability for getting a measurement at least as significant as 0.207 that was found in the 100-ms search is 0.58. In other words, under the null hypothesis, 1 in 1.7 sets of 59 on-source searches will result in a most significant excess with a binomial probability at least as significant as 0.207. And, as with the 25-ms result, this level of significance for the 100-ms search result is consistent with the null hypothesis.

Also shown in Figs. 3 and 4 is a curve indicating the excess needed for a $\sim$1% confidence in the null hypothesis. At each local probability, the curve gives the cumulative number of events needed to obtain a $\sim$1% final probability under the null hypothesis, given 59 on-source pairs.

B. Maximum likelihood ratio based tests

A maximum likelihood ratio test [56] for detecting a GW signature associated with a sample of multiple triggers was derived in [57]. (It was shown there that [53] is a special case of the maximum likelihood ratio approach.) The method proposed in [57] cannot be applied directly to the entire GRB sample described above since the largest crosscorrelation values were obtained in different ways for H1-H2 and H1-L1 (H2-L1) (cf. Sec. IV C). In the following, we will only use the largest crosscorrelations from H1-H2 on-source segments. This reduces the total number of GRB on-source segments used in this test to 35.

Let the largest crosscorrelation from the i^{th} GRB on-source segment be denoted as $cc_{\max,i}$. If we do not use any prior probability distribution for the properties of GW signals associated with GRBs, the maximum likelihood ratio detection statistic is simply the average of the largest crosscorrelation values from the GRB set,

$$\chi = \frac{1}{N_{\text{GRB}}} \sum_i cc_{\max,i}, \tag{7}$$

where N_{GRB} is the number of H1-H2 GRB on-source segments used. We call χ the *sum-max* statistic.

To build in robustness against instrumental noise artefacts, such as short-duration transients, we replace the sum-max statistic, which was derived for the ideal case of Gaussian and stationary noise, by a nonparametric counterpart. The on-source and off-source largest crosscorrelation values are pooled into two separate sets and the Wilcoxon rank-sum test [58] is used for the null hypothesis that the two sets of samples were drawn from the same underlying true distribution.

The cumulative distribution of the on-source and off-source largest crosscorrelations from the 100-ms search are shown in Fig. 5. Application of the rank-sum test shows that the significance of the null hypothesis is 0.64. This implies that one out of 1.6 trials can show a false positive detection at this significance threshold. Assuming that GRB triggers occur at a rate of one per day, 1 yr of observation would contain approximately 10 collections of 35 GRBs. In order to achieve a low false detection probability, we would require a much lower significance, such as ≤ 0.01, in order to reject the null hypothesis.

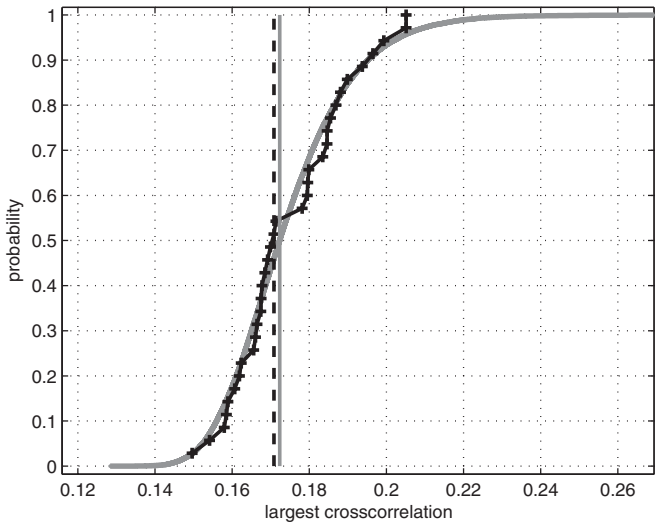

FIG. 5. The cumulative distributions of the on-source (solid black with + marker) and off-source (solid gray) largest H1-H2 crosscorrelations from the 100-ms search. The vertical lines denote the locations of the medians of the off-source (gray) and on-source (black, dashed) samples.

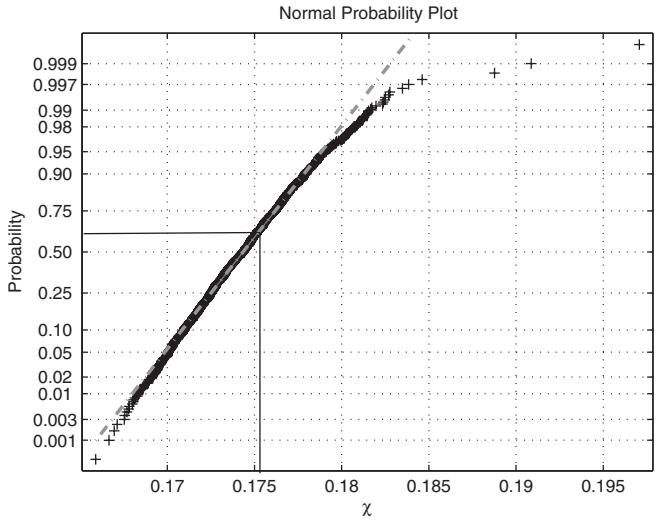

FIG. 6. Plot of the cumulative distribution function of the off-source values of the sum-max statistic χ. The dashed line shows the best fit normal distribution. The solid horizontal and vertical lines indicate the location of the on-source values of $\chi_{\rm on}$ and the corresponding cumulative probability. The on-source value was $\chi_{\rm on} = 0.1753$, which yields a cumulative probability of 0.64 or an empirical significance of $1 - 0.64 = 0.36$.

As a further check, we also compute the empirical significance of the on-source value of χ with respect to the set of off-source χ values. Values of the off-source χ statistic were calculated by pooling the largest crosscorrelations from the H1-H2 off-source segments, then dividing this pool into subsets, each of which had $N_{\rm GRB}$ number of elements. For each of these subsets, the χ statistic was calculated using Eq. (7). The empirical significance is defined as the fraction of off-source χ values greater than or equal to the on-source χ value. The empirical significance has more scatter than a significance computed with a *known* null distribution since we only have a finite number of off-source values. However, the number of off-source values in this analysis is large enough that we can ignore the associated error.

The mean and standard deviation of the off-source sum-max sample were 0.1744 and 0.0029, respectively. The on-source value of sum-max was $\chi_{\rm on} = 0.1753$. Figure 6 shows the distribution of the off-source values of the test statistic. The empirical significance of the null hypothesis is 0.36. Following the discussion above, it is clear that this result is consistent with no detection.

VI. SINGLE-GRB LIMITS

Simulations were done to estimate the sensitivity of the search method to incident GW burst signals. This process was limited by the fact that the theoretical waveforms of the GW burst signals associated with GRBs were not known. Other unknown quantities were: the polarization of the waves, the orientation of the source relative to the observer, and the redshifts of most of the GRBs. Conscious of these limitations, we proceed to set upper limits on the root-sum-square amplitude ($h_{\rm rss}$) of GW burst signals incident on the interferometers during the on-source times by using simulated waveforms with burstlike characteristics, adding these waveforms to the raw IFO data streams, and measuring the resulting crosscorrelations.

The antenna response of an IFO to incident, independent gravitational-wave strains, $h_+(t)$ and $h_\times(t)$, depends on the relative position of the source in the sky and the polarization of the wave [59]:

$$h(t) = F_+(\theta, \phi, \psi)h_+(t) + F_\times(\theta, \phi, \psi)h_\times(t), \quad (8)$$

where (θ, ϕ) is the position of the source relative to the IFO's zenith and x-arm, respectively; ψ is the polarization angle of the gravitational-wave; and $F_+(\theta, \phi, \psi)$, $F_\times(\theta, \phi, \psi)$ are the corresponding "plus" and "cross" antenna factors. For most of the GRBs analyzed, the position, (θ, ϕ), was known. The polarization angle, ψ, however, was an unknown parameter for all of the GRBs. Since the antenna factor is used in the simulations, upper limits were not set for GRBs which did not have well-defined positions. The polarization-averaged antenna factor is defined as

$$F_{\rm ave}(\theta, \phi) = \sqrt{\frac{F_+^2 + F_\times^2}{2}} = \sqrt{\langle F_+^2 \rangle_\psi} = \sqrt{\langle F_\times^2 \rangle_\psi}. \quad (9)$$

We used sine-Gaussians as the simulated waveforms for $h_+(t)$ and cosine-Gaussians for $h_\times(t)$ in Eq. (8):

$$h_+(t) = h_{+,0} \sin(2\pi f_0 t) \exp\left(\frac{-(2\pi f_0 t)^2}{2Q^2}\right), \quad (10)$$

$$h_\times(t) = h_{\times,0} \cos(2\pi f_0 t) \exp\left(\frac{-(2\pi f_0 t)^2}{2Q^2}\right), \quad (11)$$

where f_0 is the central frequency of the sine-Gaussian and cosine-Gaussian, $h_{+,0}$ and $h_{\times,0}$ are the amplitude parameters of the + and × polarization signals, respectively, and Q is a dimensionless constant which represents roughly the number of cycles with which the waveform oscillates with more than half of the peak amplitude. The root-sum-squared (rss) amplitude of $h_+(t)$ and $h_\times(t)$ is related to these parameters via

$$\sqrt{\int |h_+(t)|^2 dt} \approx h_{+,0}\sqrt{\frac{Q}{4\sqrt{\pi} f_0}} \quad \text{for} \quad Q \gtrsim 3, \quad (12)$$

$$\sqrt{\int |h_\times(t)|^2 dt} \approx h_{\times,0}\sqrt{\frac{Q}{4\sqrt{\pi} f_0}} \quad \text{for} \quad Q \gtrsim 3. \quad (13)$$

Using these waveforms for $h_+(t)$ and $h_\times(t)$, we simulated circularly polarized GW waves by setting the sine-Gaussian and cosine-Gaussian amplitudes equal to each other, $h_{+,0} = h_{\times,0} \equiv h_0$. To simulate linearly polarized

waves, we set $h_{\times,0} = 0$. In the discussion that follows, we define the $h_{\rm rss}$ of a simulated waveform as

$$h_{\rm rss} = \sqrt{\int (|h_+(t)|^2 + |h_\times(t)|^2) dt}. \quad (14)$$

Since the polarization angle, ψ, was not known for any GRB, a random polarization angle from 0 to 360 degrees was generated for each simulated waveform event. In the case of LHO-LLO simulations, the source position-dependent difference in the polarization angles at LHO and LLO—due to the nonaligned detector arms—was taken into account. Finally, before adding the attenuated waveform given by Eq. (8) into an IFO's raw data stream, it was first calibrated using the measured response function of the IFO.

Following the procedure outlined above, simulated sine-Gaussians with different frequencies and $h_{\rm rss}$ values were added to each IFO on-source data at known times. Randomness in the injection times of the order of the crosscorrelation length was introduced to simulate the fact that the relative time of the GW signal within the 180-second search window was not known. Data with injected signals were then conditioned using the procedure outlined in Sec. IV B. The search was then applied to the data near the injection times—not to the entire 180-second on-source segment—to find the largest crosscorrelations around the injection times. This simulation procedure resulted in the determination of the probability density, $p(cc|h_{\rm rss})$, for measuring a crosscorrelation, cc, corresponding to a signal injected in an on-source segment with a certain $h_{\rm rss}$ value.

The method used to set upper limits on $h_{\rm rss}$ follows the standard recipe for setting frequentist upper limits [60]. If $p(cc|h_{\rm rss})$ is the probability density for measuring a cross-correlation, cc, in an on-source segment given a signal with a certain $h_{\rm rss}$ value, then the 90% upper limit curve can be constructed from the set $(cc_{90}, h_{\rm rss})$, such that

$$0.90 = \int_{cc_{90}}^{\infty} p(cc|h_{\rm rss}) d(cc). \quad (15)$$

Examples of upper limit curves obtained through this procedure are shown in Fig. 7, with one curve corresponding to linear polarization, and the other curve corresponding to circular polarization. These curves were obtained using the H1-H2 on-source data for GRB 050306; 150-Hz, Q = 8.9 sine-Gaussians; and a 25-ms crosscorrelation length. Each curve shows the $h_{\rm rss}$ value of the simulated waveform versus cc_{90}, the crosscorrelation value at which 90% of the measured crosscorrelation values were larger [see Eq. (15)]. The data was fitted with a four-parameter sigmoid function,

$$cc_{90} = p_1 + \frac{1 - p_1}{p_4(1 + \exp[-p_2(\log_{10}(h_{\rm rss}) - p_3)])}, \quad (16)$$

where parameter p_1 defined the asymptote of cc_{90} at small

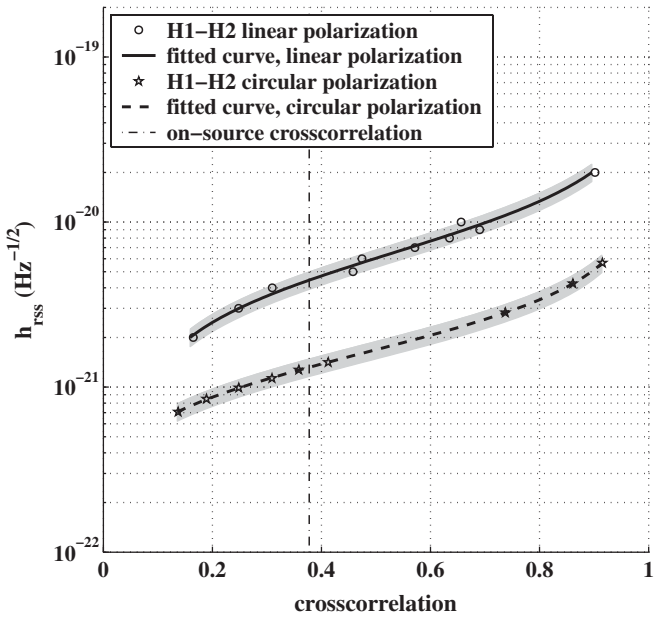

FIG. 7. Examples of upper limit curves that were used to set upper limits on $h_{\rm rss}$ using linear and circular polarizations. These were the upper limit curves for the H1-H2 IFO pair, for GRB 050306, using sine-Gaussians with Q = 8.9 and $f_0 = 150$ Hz. The shaded regions indicate the total 1σ uncertainty in the $h_{\rm rss}$ value.

values of $h_{\rm rss}$, p_4 tracked the asymptote of cc_{90} at large values of $h_{\rm rss}$ (i.e. $p_4 \approx 1/\text{asymptote}$), p_3 was the value of $h_{\rm rss}$ which gave a midrange value of cc_{90}, and p_2 defined the slope of the curve. The largest crosscorrelation found in the on-source segment is also shown in Fig. 7 (vertical dashed line). The 90% $h_{\rm rss}$ upper limit, before uncertainties, was found by evaluating the upper limit curve, which is the inverse of Eq. (16), at the largest on-source cross-correlation value found in the search.

The curves in Fig. 7 also show the estimated total 1σ uncertainty in the measurement of the $h_{\rm rss}$ values. The uncertainty in the $h_{\rm rss}$ values comes from measured random and systematic errors in the calibration parameters that were used to calibrate the simulated waveforms, and also from the statistical errors which come from the simulation procedure. Depending on which science run and IFO pair is being considered, the total 1σ uncertainty from all these sources ranged from ~10% to ~13%. However, for GRB 030217 and GRB 030226, the total uncertainty was about ~22% for the H1-H2 and H1-L1 IFO pairs, due to larger calibration errors during the times of those GRBs. The final 90% $h_{\rm rss}$ upper limits were obtained by adding the corresponding total 1.28σ uncertainties to the values obtained from the upper limit curves.

The upper limits resulting from the use of Q = 8.9 sine-Gaussians and a 25-ms crosscorrelation length, for GRBs with well-localized positions, are listed in Tables II, III, and IV for linearly polarized waveforms, and in Tables V, VI, and VII for circularly polarized waveforms. Cor-

TABLE II. S4 90% upper limits on hrss of Q = 8.9 linearly polarized sine-Gaussians, in units of 10^{-21} $Hz^{-1/2}$; 25-ms cross-correlation length.

	100 Hz			150 Hz			250 Hz			554 Hz			1000 Hz			1850 Hz		
GRB date	H1-H2	H1-L1	H2-L1	H1-H2	H1-L1	H2-L1	H1-H2	H1-L1	H2-L1	H1-H2	H1-L1	H2-L1	H1-H2	H1-L1	H2-L1	H1-H2	H1-L1	H2-L1
050223	5.5	...	...	3.6	...	...	4.1	...	...	6.9	...	...	11.7	...	...	25.8	...	...
050306	7.8	6.4	12.0	5.2	5.2	8.8	5.6	6.3	9.5	9.0	12.6	16.0	16.4	24.5	30.4	31.4	61.9	82.4
050318	7.9	10.2	15.4	6.0	7.0	10.7	6.0	9.3	11.9	9.5	16.7	19.8	15.8	30.2	35.0	33.4	55.3	66.7
050319	6.6	6.8	8.3	4.7	4.9	5.7	5.4	6.1	6.2	8.1	11.1	11.0	15.5	21.1	19.8	29.7	36.9	34.9

TABLE III. S3 90% upper limits on hrss of Q = 8.9 linearly polarized sine-Gaussians, in units of 10^{-20} $Hz^{-1/2}$; 25-ms cross-correlation length.

	100 Hz			150 Hz			250 Hz			554 Hz			1000 Hz			1850 Hz		
GRB date	H1-H2	H1-L1	H2-L1	H1-H2	H1-L1	H2-L1	H1-H2	H1-L1	H2-L1	H1-H2	H1-L1	H2-L1	H1-H2	H1-L1	H2-L1	H1-H2	H1-L1	H2-L1
031108	6.5	...	...	3.6	...	...	3.6	...	...	4.2	...	...	6.7	...	...	19.7	...	...
031109a	4.8	...	...	2.9	...	...	2.9	...	...	3.6	...	...	6.0	...	...	14.7	...	...
031220	5.7	...	...	3.3	...	...	3.0	...	...	3.7	...	...	6.3	...	...	14.7	...	...

TABLE IV. S2 90% upper limits on hrss of Q = 8.9 linearly polarized sine-Gaussians, in units of 10^{-19} $Hz^{-1/2}$; 25-ms cross-correlation length.

	100 Hz			150 Hz			250 Hz			554 Hz			1000 Hz			1850 Hz		
GRB date	H1-H2	H1-L1	H2-L1	H1-H2	H1-L1	H2-L1	H1-H2	H1-L1	H2-L1	H1-H2	H1-L1	H2-L1	H1-H2	H1-L1	H2-L1	H1-H2	H1-L1	H2-L1
030217	...	...	4.4	...	...	2.2	...	...	1.0	...	...	1.6	...	...	4.4	...	...	10.2
030226	7.7	3.5	5.4	3.4	1.6	2.2	1.00	0.68	0.63	1.3	1.1	0.81	2.6	2.4	1.4	7.1	6.6	2.7
030320a	7.2	2.1	7.1	2.5	1.1	2.2	0.69	0.58	0.71	1.0	1.1	1.3	1.6	2.9	3.1	3.8	6.0	5.6
030323a	5.1	3.1	6.4	2.5	1.7	2.9	1.1	0.99	1.5	1.7	2.3	3.3	2.6	6.1	7.2	6.0	11.4	13.4
030323b	4.6	1.8	5.2	1.7	0.94	1.8	0.64	0.45	0.81	0.92	0.82	1.5	1.3	1.8	2.4	3.0	3.5	4.8
030324	9.2	...	...	4.7	...	...	1.6	...	...	2.0	...	...	3.3	...	...	7.9	...	...
030325	2.8	1.7	3.0	1.3	0.80	1.5	0.55	0.48	0.76	0.89	1.0	1.5	1.3	2.0	2.4	3.2	4.9	5.3
030326	10.2	3.9	9.6	4.4	2.1	3.7	1.4	0.94	1.2	2.0	1.6	1.9	3.1	3.4	3.1	8.4	8.1	6.3
030329a	4.6	...	...	2.4	...	...	1.1	...	...	1.8	...	...	3.0	...	...	7.6	...	...
030329b	2.8	...	...	1.1	...	...	0.31	...	...	0.55	...	...	0.89	...	...	2.0	...	...
030331	...	3.4	...	...	1.6	...	...	0.85	...	...	2.0	...	...	3.4	...	...	8.0	...
030405	2.1	1.4	3.1	1.0	0.80	1.3	0.34	0.42	0.51	0.59	0.76	0.97	0.87	2.0	2.2	2.0	4.8	4.5
030406	...	1.2	...	...	0.67	...	...	0.42	...	...	0.77	...	...	1.7	...	...	4.4	...
030413	...	...	1.6	...	...	0.85	...	...	0.50	...	...	0.89	...	...	2.3	...	...	4.4
030414	1.4	...	...	0.91	...	...	0.32	...	...	0.39	...	...	0.70	...	...	1.6	...	...

responding limits from the use of a 100-ms crosscorrelation length are listed in Tables VIII, IX, and X, and in Tables XI, XII, and XIII. It can be seen that the upper limits for the two crosscorrelation lengths do not differ much for the waveforms that were used. The upper limits for $f_0 =$ 250 Hz and 25-ms crosscorrelation length are plotted in Figs. 8 and 9 for linear and circular polarizations, respectively. The improvement in sensitivity from the S2 to S4 runs can be seen in these plots. The best upper limits from the three science runs are given in Table XIV. From the S2 to the S4 run, there was an improvement in sensitivity by about an order of magnitude.

TABLE V. S4 90% upper limits on hrss of Q = 8.9 circularly polarized sine-Gaussians, in units of 10^{-21} $Hz^{-1/2}$; 25-ms cross-correlation length.

	100 Hz			150 Hz			250 Hz			554 Hz			1000 Hz			1850 Hz		
GRB date	H1-H2	H1-L1	H2-L1	H1-H2	H1-L1	H2-L1	H1-H2	H1-L1	H2-L1	H1-H2	H1-L1	H2-L1	H1-H2	H1-L1	H2-L1	H1-H2	H1-L1	H2-L1
050223	1.6	...	...	1.1	...	...	1.2	...	...	2.0	...	...	3.5	...	...	6.7	...	...
050306	2.2	1.4	2.6	1.5	1.1	1.8	1.6	1.4	2.0	2.6	2.6	3.3	4.5	5.0	6.2	8.5	14.2	17.6
050318	2.2	2.2	3.1	1.6	1.5	2.2	1.6	1.9	2.4	2.6	3.5	4.0	4.6	6.1	6.9	8.8	11.1	13.1
050319	1.8	1.8	2.3	1.4	1.3	1.6	1.5	1.7	1.8	2.4	3.1	3.0	4.3	5.5	5.2	8.2	10.0	9.9

TABLE VI. S3 90% upper limits on hrss of Q = 8.9 circularly polarized sine-Gaussians, in units of 10^{-21} $Hz^{-1/2}$; 25-ms crosscorrelation length.

	100 Hz			150 Hz			250 Hz			554 Hz			1000 Hz			1850 Hz		
GRB date	H1-H2	H1-L1	H2-L1	H1-H2	H1-L1	H2-L1	H1-H2	H1-L1	H2-L1	H1-H2	H1-L1	H2-L1	H1-H2	H1-L1	H2-L1	H1-H2	H1-L1	H2-L1
031108	19.0	...	...	11.3	...	...	10.9	...	...	12.5	...	...	20.4	...	...	51.5	...	...
031109a	14.7	...	...	8.8	...	...	8.5	...	...	10.6	...	...	17.3	...	...	42.2	...	...
031220	14.4	...	...	10.1	...	...	8.9	...	...	10.8	...	...	18.4	...	...	42.7	...	...

TABLE VII. S2 90% upper limits on hrss of Q = 8.9 circularly polarized sine-Gaussians, in units of 10^{-20} $Hz^{-1/2}$; 25-ms crosscorrelation length.

	100 Hz			150 Hz			250 Hz			554 Hz			1000 Hz			1850 Hz		
GRB date	H1-H2	H1-L1	H2-L1	H1-H2	H1-L1	H2-L1	H1-H2	H1-L1	H2-L1	H1-H2	H1-L1	H2-L1	H1-H2	H1-L1	H2-L1	H1-H2	H1-L1	H2-L1
030226	22.2	11.0	18.0	9.2	5.0	6.9	2.9	2.1	1.9	3.7	3.3	2.6	7.1	7.1	4.1	20.3	20.3	7.2
030320a	21.9	7.0	26.6	7.3	3.6	7.9	2.0	1.9	2.2	2.9	3.3	4.1	4.6	9.5	10.1	10.7	17.3	16.1
030323a	16.1	...	...	7.9	...	...	3.6	...	...	5.6	...	...	7.9	...	...	18.5	...	...
030323b	13.4	4.9	15.5	4.9	2.5	5.1	1.8	1.2	2.3	2.7	2.4	4.0	3.7	5.1	6.6	8.5	9.2	12.3
030324	28.0	...	...	13.3	...	...	4.3	...	...	5.6	...	...	9.4	...	...	22.2	...	...
030325	9.0	4.3	9.5	4.0	2.0	4.2	2.0	1.2	2.4	3.1	2.8	4.4	4.3	5.3	6.7	10.2	12.2	15.0
030326	29.7	15.1	39.9	12.4	8.1	14.9	4.0	3.5	4.8	5.8	5.8	7.6	9.6	12.1	11.7	24.2	25.8	19.7
030329a	13.8	...	...	7.3	...	...	3.3	...	...	5.1	...	...	8.2	...	...	21.6	...	...
030329b	8.8	...	...	3.2	...	...	0.90	...	...	1.5	...	...	2.4	...	...	5.9	...	...
030331	...	7.1	...	...	3.5	...	...	1.8	...	...	4.3	...	...	7.3	...	...	17.4	...
030405	6.2	3.4	8.2	2.9	2.0	3.4	0.99	1.1	1.3	1.6	2.0	2.5	2.5	5.1	5.4	5.9	11.3	10.7
030406	...	2.8	...	...	1.5	...	...	0.90	...	...	1.8	...	...	4.0	...	...	10.0	...
030413	...	...	4.1	...	...	2.2	...	...	1.3	...	...	2.4	...	...	6.0	...	...	11.0
030414	4.1	...	...	2.6	...	...	0.82	...	...	1.1	...	...	1.9	...	...	4.6	...	...

TABLE VIII. S4 90% upper limits on hrss of Q = 8.9 linearly polarized sine-Gaussians, in units of $10^{-21}Hz^{-1/2}$; 100-ms crosscorrelation length.

	100 Hz			150 Hz			250 Hz			554 Hz			1000 Hz			1850 Hz		
GRB date	H1-H2	H1-L1	H2-L1	H1-H2	H1-L1	H2-L1	H1-H2	H1-L1	H2-L1	H1-H2	H1-L1	H2-L1	H1-H2	H1-L1	H2-L1	H1-H2	H1-L1	H2-L1
050223	5.6	...	...	4.1	...	...	4.8	...	...	8.0	...	...	14.5	...	...	30.9	...	...
050306	6.9	6.7	12.6	4.9	5.8	9.1	5.6	7.6	10.4	9.1	13.8	17.3	16.0	28.0	34.0	30.0	74.1	91.8
050318	7.4	9.7	12.5	5.9	7.4	10.3	6.4	9.9	11.8	10.7	17.5	17.9	18.4	33.2	34.1	33.3	63.4	64.5
050319	5.5	6.0	9.6	4.6	4.6	7.2	5.2	6.5	8.4	8.8	11.4	14.4	15.2	21.3	25.1	30.1	34.7	48.3

TABLE IX. S3 90% upper limits on hrss of Q = 8.9 linearly polarized sine-Gaussians, in units of $10^{-20}Hz^{-1/2}$; 100-ms cross-correlation length.

	100 Hz			150 Hz			250 Hz			554 Hz			1000 Hz			1850 Hz		
GRB date	H1-H2	H1-L1	H2-L1	H1-H2	H1-L1	H2-L1	H1-H2	H1-L1	H2-L1	H1-H2	H1-L1	H2-L1	H1-H2	H1-L1	H2-L1	H1-H2	H1-L1	H2-L1
031108	6.0	...	...	3.6	...	...	3.8	...	...	4.5	...	...	7.9	...	...	20.1	...	...
031109a	4.4	...	...	2.7	...	...	2.9	...	...	3.5	...	...	6.1	...	...	15.1	...	...
031220	5.0	...	...	3.0	...	...	3.0	...	...	4.1	...	...	7.0	...	...	15.8	...	...

It can also be seen from Figs. 8 and 9 that, for most of the GRB source positions, the circular polarization limits are better than the linear polarization limits by about a factor of 3.5. This is always true in the case of H1-H2 upper limits since waveforms at the two coaligned LHO IFOs were always in phase (after calibrations). For LHO-LLO upper limits, there were two cases, GRB 030217 and 030323a, in which the positions of the GRBs relative to the IFOs were such that circularly polarized waveforms at LHO and LLO were sufficiently out of phase so that upper limits for circular polarization were not determinable for those GRBs.

TABLE X. S2 90% upper limits on hrss of Q = 8.9 linearly polarized sine-Gaussians, in units of $10^{-19}\mathrm{Hz}^{-1/2}$; 100-ms cross-correlation length.

	100 Hz			150 Hz			250 Hz			554 Hz			1000 Hz			1850 Hz		
GRB date	H1-H2	H1-L1	H2-L1	H1-H2	H1-L1	H2-L1	H1-H2	H1-L1	H2-L1	H1-H2	H1-L1	H2-L1	H1-H2	H1-L1	H2-L1	H1-H2	H1-L1	H2-L1
030217	...	...	4.0	...	...	2.0	...	...	0.94	...	...	1.5	...	...	4.1	...	...	9.5
030226	7.3	3.1	5.3	3.2	1.5	2.1	1.1	0.65	0.62	1.4	1.0	0.85	2.6	2.4	1.4	7.1	6.5	2.7
030320a	6.7	2.3	6.8	2.5	1.3	2.3	0.76	0.67	0.70	1.0	1.2	1.4	1.6	3.6	3.5	4.1	7.2	5.8
030323a	5.3	2.7	5.6	3.0	1.5	2.5	1.2	0.86	1.4	1.8	2.2	3.0	2.7	5.5	7.0	6.4	10.0	12.4
030323b	5.1	1.8	4.9	2.0	0.95	1.7	0.77	0.47	0.79	1.1	0.90	1.6	1.6	1.9	2.5	3.9	3.7	5.0
030324	8.7	...	...	4.6	...	...	1.5	...	...	2.0	...	...	3.7	...	...	8.0	...	...
030325	2.9	1.5	3.4	1.4	0.78	1.6	0.63	0.46	0.90	1.0	1.00	1.9	1.5	1.9	2.9	3.7	4.6	6.6
030326	9.0	3.0	7.4	4.2	1.8	3.1	1.3	0.81	0.98	1.9	1.5	1.8	3.7	3.1	2.9	8.6	6.8	5.7
030329a	4.4	...	...	2.5	...	...	1.2	...	...	2.1	...	...	3.0	...	...	8.6	...	...
030329b	2.6	...	...	1.2	...	...	0.34	...	...	0.56	...	...	0.94	...	...	2.2	...	...
030331	...	3.5	...	...	1.7	...	...	0.97	...	...	2.1	...	...	4.1	...	...	10.3	...
030405	2.3	1.2	2.6	1.3	0.76	1.1	0.46	0.40	0.47	0.73	0.73	0.90	1.2	1.8	1.9	2.7	4.4	4.0
030406	...	1.2	...	...	0.73	...	...	0.45	...	...	0.87	...	...	1.9	...	...	5.0	...
030413	...	...	1.7	...	...	0.94	...	...	0.61	...	...	1.1	...	...	2.9	...	...	5.4
030414	1.3	...	...	0.89	...	...	0.30	...	...	0.43	...	...	0.74	...	...	1.7	...	...

TABLE XI. S4 90% upper limits on hrss of Q = 8.9 circularly polarized sine-Gaussians, in units of 10^{-21} $\mathrm{Hz}^{-1/2}$; 100-ms crosscorrelation length.

	100 Hz			150 Hz			250 Hz			554 Hz			1000 Hz			1850 Hz		
GRB date	H1-H2	H1-L1	H2-L1	H1-H2	H1-L1	H2-L1	H1-H2	H1-L1	H2-L1	H1-H2	H1-L1	H2-L1	H1-H2	H1-L1	H2-L1	H1-H2	H1-L1	H2-L1
050223	1.7	...	...	1.3	...	...	1.5	...	...	2.4	...	...	4.4	...	...	8.3	...	...
050306	2.0	1.5	2.6	1.5	1.2	1.9	1.7	1.7	2.2	2.8	3.1	3.7	4.9	6.0	7.0	9.3	16.3	19.1
050318	2.2	2.1	2.8	1.7	1.6	2.2	1.9	2.1	2.4	3.0	4.0	4.2	5.5	6.9	7.4	10.3	12.7	14.0
050319	1.7	1.6	2.5	1.4	1.3	1.9	1.6	1.7	2.2	2.6	3.2	3.8	4.7	5.7	6.7	9.1	10.3	12.8

TABLE XII. S3 90% upper limits on hrss of Q = 8.9 circularly polarized sine-Gaussians, in units of $10^{-21}\mathrm{Hz}^{-1/2}$; 100-ms crosscorrelation length.

	100 Hz			150 Hz			250 Hz			554 Hz			1000 Hz			1850 Hz		
GRB date	H1-H2	H1-L1	H2-L1	H1-H2	H1-L1	H2-L1	H1-H2	H1-L1	H2-L1	H1-H2	H1-L1	H2-L1	H1-H2	H1-L1	H2-L1	H1-H2	H1-L1	H2-L1
031108	18.4	...	...	11.5	...	...	11.8	...	...	14.0	...	...	23.2	...	...	61.0	...	...
031109a	13.5	...	...	8.5	...	...	8.7	...	...	11.3	...	...	19.0	...	...	47.6	...	...
031220	12.1	...	...	9.4	...	...	8.8	...	...	11.6	...	...	20.5	...	...	49.1	...	...

TABLE XIII. S2 90% upper limits on hrss of Q = 8.9 circularly polarized sine-Gaussians, in units of 10^{-20} $\mathrm{Hz}^{-1/2}$; 100-ms crosscorrelation length.

	100 Hz			150 Hz			250 Hz			554 Hz			1000 Hz			1850 Hz		
GRB date	H1-H2	H1-L1	H2-L1	H1-H2	H1-L1	H2-L1	H1-H2	H1-L1	H2-L1	H1-H2	H1-L1	H2-L1	H1-H2	H1-L1	H2-L1	H1-H2	H1-L1	H2-L1
030226	22.1	9.6	16.7	9.8	4.7	6.1	3.1	2.0	1.9	4.1	3.2	2.6	7.8	7.2	4.5	21.2	19.6	8.0
030320a	21.0	7.4	24.7	7.7	4.1	7.6	2.2	2.2	2.4	3.3	4.0	4.5	5.3	11.4	10.8	12.3	21.7	18.3
030323a	16.7	...	...	8.8	...	...	4.0	...	...	6.3	...	...	9.3	...	...	21.8	...	...
030323b	14.8	4.8	14.4	5.9	2.6	4.8	2.2	1.3	2.4	3.3	2.5	4.4	4.7	5.3	7.4	10.9	10.4	14.1
030324	27.0	...	...	13.9	...	...	4.7	...	...	6.3	...	...	10.7	...	...	24.7	...	...
030325	9.7	3.7	9.9	4.6	2.0	4.5	2.2	1.2	2.8	3.5	2.6	5.4	5.2	5.1	8.4	12.3	12.5	19.1
030326	28.3	11.0	28.6	13.0	6.3	10.9	4.3	2.9	3.7	6.3	5.0	6.2	10.6	10.6	10.2	26.4	23.2	18.3
030329a	13.7	...	...	7.8	...	...	3.6	...	...	5.8	...	...	9.5	...	...	24.8	...	...
030329b	8.1	...	...	3.3	...	...	1.0	...	...	1.7	...	...	2.8	...	...	6.7	...	...
030331	...	7.4	...	...	3.7	...	...	2.1	...	...	4.9	...	...	8.6	...	...	20.6	...
030405	7.1	3.1	6.8	3.7	1.9	2.9	1.3	1.1	1.2	2.1	1.9	2.3	3.3	5.0	5.2	7.8	11.6	10.4
030406	...	2.8	...	...	1.7	...	...	1.0	...	...	2.0	...	...	4.6	...	...	11.6	...
030413	...	...	4.3	...	...	2.4	...	...	1.5	...	...	2.8	...	...	7.3	...	...	13.5
030414	4.1	...	...	2.7	...	...	0.91	...	...	1.3	...	...	2.2	...	...	5.2	...	...

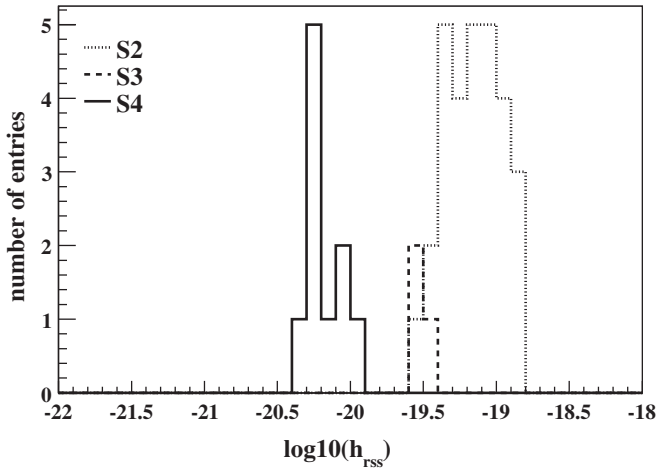

FIG. 8. Progression of h_{rss} upper limits from the S2 to S4 LIGO runs for linearly polarized sine-Gaussian waveforms; 25-ms crosscorrelation.

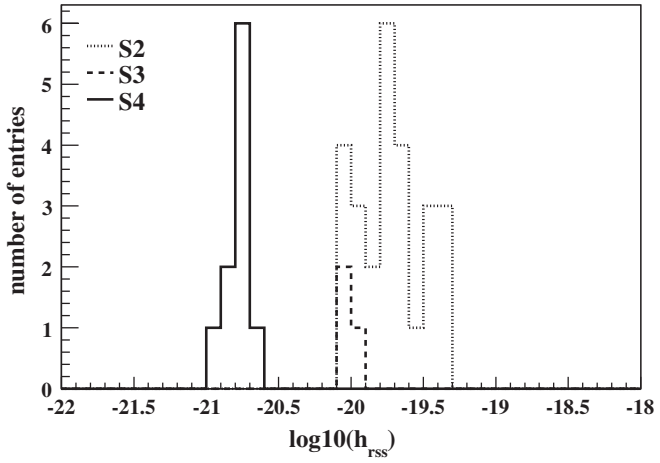

FIG. 9. Progression of h_{rss} upper limits from the S2 to S4 LIGO runs for circularly polarized sine-Gaussian waveforms; 25-ms crosscorrelation.

TABLE XIV. Best 90% h_{rss} upper limits resulting from a search of GW signals from GRBs occurring during the three LIGO runs; 25-ms crosscorrelation analysis ($\mathrm{Hz}^{-1/2}$).

Run	$h_{\mathrm{rss},90}$ (circular)	$h_{\mathrm{rss},90}$ (linear)	f_0
S4	1.1×10^{-21} (050306)	3.6×10^{-21} (050223)	150 Hz
S3	8.5×10^{-21} (031109A)	2.9×10^{-20} (031109A)	250 Hz
S2	8.2×10^{-21} (030414)	3.1×10^{-20} (030329B)	250 Hz

VII. CONSTRAINING GRB POPULATION MODELS

The approach of combining multiple GRBs to look for a GW signature associated with a sample of GRBs was described in Sec. V. Having established that the null hypothesis is quite significant, i.e. that we cannot claim the detection of an association between GWs and the GRB population at a high enough confidence, we turn to setting constraints on the parameters of GRB population models. The method is summarized below and described in detail in [61].

For a pair of detectors, it can be shown that only three scalar parameters associated with a GW signal are sufficient to determine the distribution of largest crosscorrelations. The parameters are the matched filtering *signal-to-noise ratios* (SNRs) of the strain signals in individual detectors and the angle between the two strain signal vectors (as defined by the Euclidean inner product). In the following, a *source population model* is the joint probability distribution function of these three parameters.

Our approach to putting constraints on source population models follows the standard frequentist upper limit procedure (cf. Sec. VI). In this case, let $P(\chi|Z_{\mathrm{source}})$ be the marginal cumulative probability density function of the sum-max statistic, χ, given the population model Z_{source}, and let χ_α be such that $P(\chi_\alpha|Z_{\mathrm{source}}) = 1 - \alpha$, where $0 < \alpha < 1$, and $1 - \alpha$ is the desired confidence level. If the *observed* value of χ is greater than or equal to χ_α, the corresponding model Z_{source} is accepted. It is rejected when $\chi < \chi_\alpha$. To obtain the marginal distribution of χ, we first construct its conditional distribution for a set of N_{GRB} values for the scalar parameters above, where N_{GRB} is the number of H1-H2 GRB on-source segments. The marginal distribution of χ for a given source population model can then be estimated by randomly drawing values of the scalar parameters followed by drawing χ from the corresponding conditional distribution.

Since we use only the H1-H2 pair, which are perfectly aligned, the angle between the strain responses is zero. Further, for narrowband signals, the SNR values for H1 and H2 can be related by the measurable ratio of their calibrated noise power spectral densities (PSDs). Hence, only one parameter, which we chose to be the SNR, ρ, of the signal in H1, is required. Thus, the source population model, Z_{source}, is simply the univariate distribution of ρ. An additional point that needs to be accounted for is the variation in the sensitivities of H1 and H2, both within the runs as well as the significant improvements from one run to the next. This is done by fixing a *fiducial* noise PSD, $S^{(0)}(f)$, and approximating the PSD of H1 for each GRB as simply a scaled version of it. We set the fiducial noise PSD to the one corresponding to the initial LIGO design sensitivity for the 4-km IFOs [62] and compute the scale factor at a fixed frequency of 200 Hz, which was approximately where most PSDs had their minimum during the S2, S3, and S4 runs.

We use the theoretical prediction of the observed redshift distribution of GRBs given in [63] to construct Z_{source} (prediction for the scenario of star formation via atomic hydrogen cooling). An alternative is to simply use the measured redshift distribution but [31,64] show that there

is a significant selection bias that affects the measured redshifts for Swift and non-Swift GRBs, both of which are used in our analysis. The model in [63] is valid for long-duration GRBs, which are expected to trace the massive star formation rate of the Universe. We fit a piecewise parabolic curve (with 3 pieces) to Fig. 1 of [63] and then use the same subsequent calculational steps given in [63] to obtain the redshift distribution for a flux-limited detector such as Swift. Fitting the star formation rate with a smooth curve allows us to extend the redshift distribution reliably to very small values of the redshift. Having obtained the distribution, we directly draw random values of the redshift, z, from it. Each redshift value is then converted to the corresponding luminosity distance D (corresponding to a Friedmann-Robertson-Walker cosmological model with $\Omega_m = 0.3$, $\Omega_\Lambda = 0.7$, and $H_0 = 72\ \mathrm{km\,sec^{-1}\,Mpc^{-1}}$).

A simple model is used for the GW emission from GRBs. We assume that GRBs are standard candles in GW that emit a fixed amount of energy, E_{GW}, isotropically with similar amounts of radiation in the two uncorrelated polarizations $+$ and $\times$. Further, neglecting the effect of redshift on the signal spectrum, we assume that the spectra of the received signals h_+ and $h_\times$ are centered at a fixed frequency of f_o in a band that is sufficiently narrow such that the noise power spectral density is approximately constant over it. In this case, the SNR is given by

$$\rho \simeq \sqrt{2} F_{\mathrm{ave}} \frac{h_{\mathrm{rss}}}{\sqrt{S^{(0)}(f_o)}}, \tag{17}$$

where we have expressed the SNR with respect to the fiducial noise PSD. Since the emission is isotropic, the energy emitted in gravitational waves is (cf. Sec. VIII A)

$$E_{\mathrm{GW}} \approx \frac{\pi^2 c^3}{G} \frac{D^2}{1+z} f_o^2 h_{\mathrm{rss}}^2. \tag{18}$$

To convert the luminosity distance, D, for a given GRB into SNR ρ, we use the normalization

$$\rho = \sqrt{2} F_{\mathrm{ave}} \rho_0 \frac{D_0}{D} \left(\frac{1+z}{1+z_0} \right)^{3/2}, \tag{19}$$

where D_0 is chosen to be the most probable luminosity distance, at the corresponding redshift z_0, and ρ_0 is the observed SNR for a GRB that occurred at D_0 with an optimal sky location and the above properties for h_+, $h_\times$, and E_{GW}. The redshift distribution predicted in [63] for Swift has a peak at $z = 1.8$, which yields $D_0 = 13.286$ Gpc. The acceptance-rejection rule above simply becomes an upper limit on the value of ρ_0. Note that, because of the scaling of noise PSDs discussed above, ρ_0 should be understood as the SNR of the strain response (for a GRB directly above the detector) that operates at design sensitivity. For GRBs that do not have direction information, random values for F_{ave} are drawn from a uniform distribution on the celestial sphere.

Finally, in terms of the upper limit, ρ_{upper}, obtained on ρ_0, we get an upper limit on E_{GW},

$$E_{\mathrm{GW}} \leq \frac{\pi^2 c^3}{G} \frac{D_0^2}{1+z_0} f_o^2 S^{(0)}(f_o) \rho_{\mathrm{upper}}^2. \tag{20}$$

For $z_0 = 1.8$, $f_o = 200$ Hz, and $\sqrt{S^{(0)}(f_o)} = 2.98 \times 10^{-23}\ \mathrm{Hz}^{-1/2}$, we get $E_{\mathrm{GW}} \leq 8.43 \times 10^{55} \rho_{\mathrm{upper}}^2$ ergs ($\equiv 47.3 \rho_{\mathrm{upper}}^2\ M_\odot c^2$).

Figure 10 shows the 90% upper limit confidence belt for ρ_0. The on-source value of sum-max was $\chi = 0.1753$ for the S2, S3, S4 GRB sample. Hence, $\rho_0 \leq 35.5$ and $E_{\mathrm{GW}} \leq 5.96 \times 10^4\ M_\odot c^2$. This limit is too high to be of any astrophysical importance. However, as discussed later, future analyses may be able to improve by orders of magnitude on this result.

Since the detectors during the S2 run were much less sensitive than S4, one may expect that dropping the S2 GRBs from the analysis can improve the upper limit. Figure 10 shows the 90% level upper limit belt obtained for the case when only the last 10 GRBs, spanning the whole of S4 and part of S3, were retained in the analysis. The corresponding value of $\chi = 0.1702$ yields an upper limit of 24.6 on ρ_0. Thus, we obtain $E_{\mathrm{GW}} \leq 2.86 \times 10^4\ M_\odot c^2$. This shows, as expected, that making judicious cuts on the sample of GRBs can lead to improvements in upper

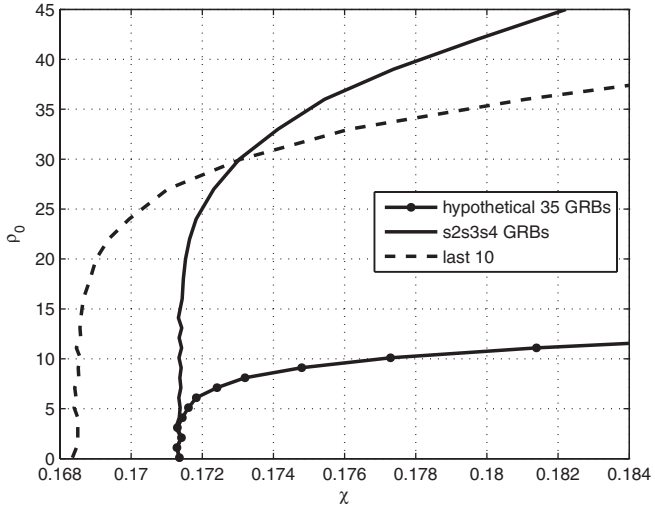

FIG. 10. Upper limit confidence belts at 90% confidence level on ρ_0, the SNR at the most probable redshift for Swift GRBs given in [63]. The solid line is the curve for all S2, S3, S4 GRBs that were used in the H1-H2 search (on-source $\chi = 0.1753$). The dashed line is the curve when only the last 10 GRBs from the above set are selected (on-source $\chi = 0.1702$). The line with filled circles is for a hypothetical scenario with 35 GRBs, all with an optimal sky location, and two identical and constant sensitivity detectors. The shifting of the curves horizontally is due to the change in the variance of χ as the number of GRBs is changed. For each value of ρ_0, 10 000 values of χ were drawn from its marginal distribution.

limits. The upper limit can probably be improved further by retaining only the S4 GRBs, but for a small number of GRBs the distribution of χ used is not valid and a more accurate calculation has to be done. In Fig. 10, we also show the upper limit confidence belt for a hypothetical scenario that is likely for the ongoing S5 run: a sample size of about 35 GRBs with the H1 and L1 detectors operating at design sensitivity. The implications of this curve are discussed in the next section.

The confidence belt construction outlined in this section is for illustrative purposes only. In particular, we have not taken into account factors such as (i) changing noise spectral shapes, (ii) red-shifting of the standard candle (K-correction) and possible systematic errors associated with the population model used. A more comprehensive investigation is planned for the S5 data.

VIII. DISCUSSION

This search is not very restrictive with respect to models for astrophysical systems which give rise to GRBs. The main assumption we have made is that the GW emission is limited in duration—we sum over periods of up to 100 ms, which is much greater than the characteristic times expected for GW burst emission in most GRB models. Given the LIGO sensitivity at the time of this search, it is not surprising that our experimental limits in this search do not place significant restrictions on the astrophysical models at present. However, given the rapid development of the field, it is not precluded that the limits presented here will provide guidance to GRB astrophysics in the near future. In any case, it is useful to get a sense for the interplay between the measured gravitational-wave strain limits for individual GRBs from Sec. VI and astrophysical models. So in this section we provide some astrophysical context to our experimental limits. We emphasize that the estimates given below are for illustration, and are not to be construed as measured astrophysical limits.

The local gravitational-wave energy flux in the two independent polarizations, $h_+(t)$ and $h_\times(t)$, is [59,65]

$$\frac{dE}{dAdt} = \frac{1}{16\pi}\frac{c^3}{G}(\dot{h}_+^2 + \dot{h}_\times^2) \tag{21}$$

which can be integrated over the duration of a burst of gravitational radiation and over a closed surface to relate the strains evaluated on the surface to the total intrinsic energy associated with a source within this volume. For a source at the center of a sphere of radius r at negligible redshift, then $dA = r^2 d\Omega$, as usual.

Since many of the GRBs in the sample are found to have significant redshifts, it is useful to generalize the above to cosmological distances. In this case, we can use the luminosity distance, D, which by definition relates the intrinsic luminosity, $\mathcal{L}$, of an isotropically emitting source to the energy flux $\mathcal{F}$ at a detector by $\mathcal{L} = \mathcal{F}(4\pi D^2)$. For a non-isotropic emitter, we replace the 4π by an integration over solid angle. We note that $\mathcal{F}$ is by definition the left-hand side of Eq. (21), and the intrinsic luminosity is $\mathcal{L} = dE_e/dt_e$. To integrate this over the signal duration at the detector, we use $dt = (1+z)dt_e$. Hence, the energy emitted in gravitational radiation is

$$\begin{aligned} E_e &= \frac{D^2}{1+z}\int d\Omega \int \mathcal{F} dt \\ &= \frac{1}{16\pi}\frac{c^3}{G}\frac{D^2}{1+z}\int d\Omega \int (\dot{h}_+^2 + \dot{h}_\times^2) dt. \end{aligned} \tag{22}$$

For negligible redshifts, $D = r$. We note that $D = D(z)$ is itself a function of the redshift, and in general depends on the cosmological model.

If the signal power at the detectors is dominated by a frequency f_o, as is the case for the sine-Gaussian waveforms introduced earlier, then Eq. (22) can be written in the approximate form

$$E_e \approx \frac{\pi}{4}\frac{c^3}{G}\frac{D^2}{1+z} f_o^2 \int d\Omega \int (h_+^2 + h_\times^2) dt, \tag{23}$$

which allows a direct relation between E_e and the observable $h_{\rm rss}$ [see Eqs. (12) and (13)]. For sine-Gaussian waveforms, the approximation is quite good for $Q \gtrsim 3$; the error is approximately $1/(1+2Q^2)$. We will assume here that the simulated waveforms are effectively local to the detectors. Specifically, the frequency f_o is the measured frequency (which is related to the source frequency f_e by $f_o = f_e/(1+z)$). Of course, some fraction of the source power might be shifted in or out of the sensitive LIGO band in frequency or expanded in time beyond our integration time. We ignore any such effect here.

A. Case I: Isotropic emission

First, we consider a simple, but unphysical, example where the radiation is emitted isotropically, with equal power in the (uncorrelated) + and × polarizations. In this case, Eq. (23) becomes

$$E_{\rm iso} \approx \frac{\pi^2 c^3}{G}\frac{D^2}{1+z} f_o^2 h_{\rm rss}^2. \tag{24}$$

Then for a LIGO sensitivity for some waveform represented by $h_{\rm rss}$, we might hope to be sensitive to a distance

$$\begin{aligned} D \approx 70\ {\rm Mpc} &\left(\frac{100\ {\rm Hz}}{f_o}\right)\left(\frac{E_{\rm iso}}{M_\odot c^2}\right)^{1/2} \\ &\times \left(\frac{10^{-21}\ {\rm Hz}^{-1/2}}{h_{\rm rss}}\right)(1+z)^{1/2} \end{aligned} \tag{25}$$

for an isotropic source which emits gravitational-wave energy $E_{\rm iso}$ (in units of solar rest energy) at detected frequency f_o.

B. Case II: Long-duration GRBs

For long-duration GRBs, we consider the scenario where such events are associated with a core collapse, perhaps involving a very massive progenitor [66]. Gravitational-wave emission has been simulated for supernova core-collapse models for relatively light ($\sim 10M_\odot$) progenitors, for example, in Refs. [36,37]. These models invoke axisymmetry, with linearly polarized strain that is proportional to $\sin^2\iota$, where ι is the angle with respect to the symmetry axis.

Integrating over the full solid angle, Eq. (23) becomes

$$E_{\rm sn} \approx \frac{8\pi^2 c^3}{15G}\frac{D^2}{1+z}\frac{f_o^2 h_{\rm rss}^2}{\sin^4\iota}. \quad (26)$$

We then find an analogous expression to Eq. (25),

$$D \approx 1\ {\rm Mpc}\left(\frac{100\ {\rm Hz}}{f_o}\right)\left(\frac{E_{\rm sn}}{10^{-4}M_\odot c^2}\right)^{1/2} \times \left(\frac{10^{-21}\ {\rm Hz}^{-1/2}}{h_{\rm rss}}\right)\sin^2\iota(1+z)^{1/2}. \quad (27)$$

As described earlier, our experimental limits correctly account for the antenna pattern associated with each GRB. Hence, no additional factors are required in the equation above if one were to use values from the tables of results. However, if one wished, for example, to apply a theoretical $h_{\rm rss}$ to a particular GRB, the antenna factors for each GRB are given in Table I.

Core-collapse simulations indicate that most of the gravitational radiation is emitted from the core bounce, and that $E_{\rm sn}$ should be at most $10^{-7}Mc^2$ [37], or even smaller [36]. For the very massive progenitors often associated with long-duration GRBs, the collapse process is uncertain. Whether there is a bounce at all, or simply a direct collapse to a black hole, depends [67] on the mass, metallicity, and angular momentum of the progenitor. In any case, there is no reason to believe that the efficiency for converting the collapse into gravitational radiation increases with the progenitor mass.

In fact, the situation for GW detection in this scenario is especially unpromising. It is natural to align the symmetry axis of the (rotating) core collapse with the direction of the gamma-ray beam. Hence, $\iota = 0$ would be along the line of sight to the detectors. For a typical gamma-ray beaming angle of half-width $\sim 10°$, then at best, where the detectors are at the edge of the beam, this would give a suppression factor of ~ 30. Finally, we note that long-duration GRBs are distant objects, with mean observed redshift of ≈ 2.4 [68]. Given their redshift distribution, the simulations to date indicate that detection of long-duration GRBs is unlikely if core bounce is the dominant radiation mechanism.

However, core collapse can potentially drive other mechanisms more favorable for gravitational radiation detection. In particular, bar mode instabilities are potentially very efficient radiators and do not suffer from the unfavorable alignment noted above for axisymmetric core bounces. Similarly, core fragmentation during collapse can lead to GW radiation from the inspiraling fragments. Reference [67] has examined these possibilities, and while the likelihood of bar instabilities or core fragmentation, along with their detailed properties, is uncertain, the resulting gravitational radiation is plausibly detectable for a nearby GRB. In such cases, Eqs. (29) and (30) might be more appropriate descriptions of the radiated energy and distance to which we can detect the source.

The nearest known GRB to date is long-duration burst GRB 980425 at $D = 35$ Mpc. From Eq. (27), LIGO detection at 35 Mpc by the method described in this paper would require an efficiency of at least $E_{\rm sn}/M_\odot c^2 \approx 10\%$ for a $1M_\odot$ system, much larger than the efficiency expected from conventional core collapse, but perhaps not unreasonable in case of bar instabilities or core fragmentation. Unfortunately, the data considered here did not include any such nearby events. For example, during the (most sensitive) S4 run, the GRB sample consisted of only 4 events, all long-duration GRBs. The most nearby of these with a measured redshift was GRB 050223 ($z = 0.5915$) at $D \approx 3.5$ Gpc. Assuming linear polarization, we can obtain an estimate for sensitivity from the 90% upper limit for GRB 050223 from Table XIV. This gives for $E_{\rm sn}$ the value $1.6 \times 10^4 M_\odot c^2$. This is in fact very close to the source luminosity maximum of c^5/G [69], which gives $2 \times 10^4 M_\odot c^2$ if sustained for 100 ms. The larger sample of GRBs in future runs will hopefully include some long-duration GRBs at smaller redshift.

C. Case III: Short-duration GRBs

Short-duration GRBs, to the extent that the population is associated with the merger of compact binary systems, offer several potentially interesting characteristics. First, such mergers are found to be relatively efficient radiators of gravitational radiation. Second, the emission pattern is not expected to be problematic. Moreover, the measured redshifts to date indicate a significant number of relatively low-z GRBs. (The average redshift was ≈ 0.4 for the 2005 sample of 5 events.) The mergers may include formation of a hypermassive neutron star [70] or a black hole with associated ringdown [71]. Finally, the merger GW emission, which is best suited to the methodology described in this paper, would be preceded by an inspiral which is potentially detectable by a sensitive, independent LIGO search based on matching inspiral waveform templates [72]. However, we have verified that the present search, while not as sensitive to inspirals as the dedicated waveform template-based search, can readily detect inspiral emission when there is sufficient signal to background in individual 25-ms or 100-ms bins. In this case, the maximum crosscorrelation occurs when the frequency of the inspiral radiation passes through the 100–300 Hz range, where the detector sensitivity is best (see Fig. 1).

Therefore, while this search is uniquely sensitive to the higher frequency, short-duration, poorly modeled gravitational waves from the merger phase, it also provides independent information on the inspiral phase. Recent estimates [34,35] place the chance for detection of a BH-NS merger at up to ~30% for a year of simultaneous LIGO and Swift operation, and ~10% for a NS-NS merger. Here, we provide an estimate for a contrived, but physically motivated, model.

We suppose that the gravitational-wave emission pattern for the merger follows that of the inspiral, that is

$$h_+ = h_o f(t)\frac{1}{2}(1+\cos^2\iota), \qquad h_\times = h_o g(t)\cos\iota \quad (28)$$

where ι is measured with respect to the axis orthogonal to the plane of the inspiral orbit. The functions $f(t)$ and $g(t)$ are orthogonal functions, for example $f(t)$ could be the sine-Gaussian form discussed earlier, while $g(t)$ is a cosine-Gaussian; h_o represents a constant amplitude. While the degree of gamma-ray beaming for short-duration GRBs is still uncertain, we suppose that the gamma rays are preferentially emitted along the angular momentum axis of the merger system. If the Earth is near the center of the gamma-ray beam, then $\iota = 0$ is along the line of sight between detector and source, which is a maximum of the assumed emission pattern, and the radiation will be circularly polarized. Returning to Eq. (23) and integrating over the full solid angle, we find in this case (with $\iota = 0$)

$$E_{\rm merge} \approx \frac{2\pi^2}{5}\frac{c^3}{G}\frac{D^2}{1+z} f_o^2 h_{\rm rss}^2. \quad (29)$$

Rewriting this for D, as before, gives

$$D \approx 44\ {\rm Mpc}\left(\frac{250\ {\rm Hz}}{f_o}\right)\left(\frac{E_{\rm merge}}{M_\odot c^2}\right)^{1/2} \times \left(\frac{10^{-21}\ {\rm Hz}^{-1/2}}{h_{\rm rss}}\right)(1+z)^{1/2}. \quad (30)$$

The comments below Eq. (27) concerning antenna factors also apply here.

There has been substantial recent progress in calculations of gravitational radiation production in various types of mergers. Numerical simulations of NS-NS mergers give [71,73,74] typical values of the radiated energy of about 0.5–1% of the total mass, or $E \approx 0.01 M_\odot c^2$. These simulations indicate that the frequency spectrum can be broad, ranging from a few hundred Hz to ~2 kHz. Perhaps the most interesting case is BH-NS mergers. Very recent calculations [75–77] indicate radiative energies ranging from $\sim 10^{-4}$ to $\sim 10^{-2}$ of the total mass, where the range is likely to reflect the very different initial conditions assumed in the simulations. While there are no short-duration GRBs in the S4 sample, we can use typical upper limits on $h_{\rm rss}$ from Table V as an indication of sensitivity. For example a $1.4 M_\odot$ NS plus $10 M_\odot$ BH binary system would have merger GW emission at frequencies starting at about 400 Hz. If this system were to radiate 1% of its rest energy into gravitational radiation at 400 Hz, the distance sensitivity would be $D \sim 5$ Mpc. The search would also be sensitive to the inspiral emission from this system at lower (~ 200 Hz) frequency.

D. Prospects

Here we discuss the future prospects for science run S5 and beyond. At the sensitivity for science run S4, the prospects for detection are clearly dominated by the possibility of a nearby GRB. While this distance scale is guided by the discussion above, we are prepared to be surprised by new mechanisms for GW emission. Nevertheless, we expect detection of individual GRBs to depend in no small part on the appearance of a ''special'' event. Thus, a data sample which includes a large number of GRBs is especially important. For science run S5, the LIGO detectors will be operating at design sensitivity and fully coincident with Swift operation. This should yield over 100 GRBs, including some with redshift measurements. And clearly, the search radius will increase in proportion to improvements in the LIGO strain sensitivity.

The results pertaining to the GRB population obtained in Sec. VII will certainly improve for the S5 run and in future observations with Advanced LIGO. To make an estimate, we look at the various factors involved in Eq. (20) for the upper limit on $E_{\rm GW}$. As a reference, we use the limit obtained here using all S2, S3, and S4 GRBs. Since most factors in Eq. (20) come as squares, moderate improvements in each has a significant overall effect.

Since the direction to each GRB will be known, it may be possible to select a subsample of, say, 35 GRBs from the sample in S5 (i.e. about the same number as the whole of S2, S3, and S4) such that $\langle F_{\rm ave}\rangle \simeq 1/\sqrt{2}$, the maximum possible. Further, assume that we use H1-L1 crosscorrelations. Figure 10 shows the confidence belt for the case of 35 optimally located GRBs and a pair of identical detectors. One can expect to get an upper limit of $\simeq 10$ on ρ_0 with this curve, which is a factor of ~3.5 better than the current limit on ρ_0.

Without altering other parameters of the analysis, therefore, we can expect 3.5^2 or, in round numbers, a factor of ~10 improvement in the upper limit on $E_{\rm GW}$ for S5. Additional improvements are possible by imposing a cut based on measured redshifts, in addition to the cut on sky positions, and by reducing the search interval from the current value of 180 s. Looking beyond S5, the most obvious source of improvement would be the ≥ 10 factor of improvement in the strain noise level when Advanced LIGO comes online around the middle of the next decade. This translates into an additional factor of ≥ 100 reduction in the upper limit. When Advanced LIGO comes online, there may be a worldwide network of GW detectors of comparable sensitivity. Besides allowing a more uniform sky coverage, resulting in a larger sample of GRBs with

optimal orientation, network analysis methods [78–80] that make more optimal use of data from multiple detectors can be used to increase the base sensitivity of the method. Finally, with enough GRBs, we could separately analyze the class of long- and short-duration bursts. Since the most probable redshift for short-duration GRBs is expected to be inherently smaller, we could obtain significantly tighter constraints on the energy emitted in gravitational waves from this class of GRBs.

The discussion above was confined to a particular model for GRB redshift distribution and GW emission. Further work is needed to develop more general analysis methods that can be applied to a wider variety of models and that take better account of prior information from existing observations.

IX. SUMMARY AND CONCLUSION

We searched for gravitational-wave bursts, targeting short GW signals with durations from $\sim$1 ms to $\sim$100 ms, associated with 39 GRBs that were detected by gamma-ray satellite experiments while the S2, S3, and S4 science runs of the LIGO experiment were in progress. To take into account the unknown onset time of the GW signal relative to the GRB trigger time, the search covered 180 s of data surrounding the GRB trigger times. These 180-s data segments from the different IFOs were cross-correlated to probe for correlated signals. We searched for an association on an individual-GRB basis, and also applied different statistical tests to search for the cumulative effect of weak GW signals. We found no evidence for gravitational-wave burst emission associated with the GRB sample examined using the different search methods.

Using simulated $Q = 8.9$ sine-Gaussian waveforms and the direction-dependent antenna response of the interferometers to a GW source, we obtained upper limits on the root-sum-square amplitude of linearly polarized and circularly polarized gravitational waves from each of 22 GRBs with well-localized positions. Associating these limits with the energy radiated by the GRB sources into gravitational radiation is inherently speculative at this stage of development of the field and depends crucially on the astrophysical scenario one adopts for the GRB progenitors. The most favorable cases considered here suggest that the LIGO sensitivity for run S4 would allow sensitivity to a solar mass-equivalent of radiated GW energy to distances of tens of Mpc.

The sample of GRBs was combined to set an upper limit on the GW energy emitted using a simple standard candle model and a theoretical redshift distribution of GRBs. Although the upper limit obtained is not astrophysically important, a straightforward and realistic extrapolation to future observations suggests that this limit can be improved by orders of magnitude. It may be possible to set a subsolar mass limit when Advanced LIGO comes online. This would put us in an astrophysically interesting regime since at least one model [81] predicts an energy loss of 0.2 solar masses for long-duration GRBs.

It is opportune that Swift will be operating and detecting GRBs at the time when the fifth science run of LIGO, S5, will be in progress. The goal for the S5 run is to collect 1 yr of coincident LHO-LLO data at the design sensitivity. Given the Swift GRB detection rate, we anticipate an S5 sample of more than 100 GRB triggers that can be used to further probe for gravitational radiation associated with GRBs. It is hoped that a large GRB sample will increase the chances for finding such an association.

ACKNOWLEDGMENTS

The authors gratefully acknowledge the support of the United States National Science Foundation for the construction and operation of the LIGO Laboratory and the Particle Physics and Astronomy Research Council of the United Kingdom, the Max-Planck-Society, and the State of Niedersachsen/Germany for support of the construction and operation of the GEO600 detector. The authors also gratefully acknowledge the support of the research by these agencies and by the Australian Research Council, the Natural Sciences and Engineering Research Council of Canada, the Council of Scientific and Industrial Research of India, the Department of Science and Technology of India, the Spanish Ministerio de Educacion y Ciencia, The National Aeronautics and Space Administration, the John Simon Guggenheim Foundation, the Alexander von Humboldt Foundation, the Leverhulme Trust, the David and Lucile Packard Foundation, the Research Corporation, and the Alfred P. Sloan Foundation. This document has been assigned LIGO Laboratory document number LIGO-P060024-07-Z.

[1] R. W. Klebesadel, I. B. Strong, and R. A. Olson, Astrophys. J. **182**, L85 (1973).
[2] G. J. Fishman, C. A. Meegan, R. B. Wilson, W. S. Paciesas, and G. N. Pendleton, in "The Compton Observatory Science Workshop" (1992), p. 26.
[3] G. Boella *et al.*, Astron. Astrophys. Suppl. Ser. **122**, 299 (1997).
[4] C. A. Meegan *et al.*, Nature (London) **355**, 143 (1992).
[5] C. Kouvelitou *et al.*, Astrophys. J. **413**, L101 (1993).
[6] E. Costa *et al.*, Nature (London) **387**, 783 (1997).
[7] J. van Paradijs *et al.*, Nature (London) **386**, 686 (1997).

[8] D. A. Frail, S. R. Kulkarni, L. Nicastro, M. Feroci, and G. B. Taylor, Nature (London) **389**, 261 (1997).
[9] M. R. Metzger *et al.*, International Astronomical Union Circular No. 6655 (1997).
[10] M. R. Metzger *et al.*, International Astronomical Union Circular No. 6676 (1997).
[11] J. S. Bloom, S. G. Djorgovski, and S. R. Kulkarni, Astrophys. J. **507**, L25 (1998).
[12] T. J. Galama *et al.*, Nature (London) **395**, 670 (1998).
[13] K. Iwamoto *et al.*, Nature (London) **395**, 672 (1998).
[14] S. R. Kulkarni *et al.*, Nature (London) **395**, 663 (1998).
[15] N. Gehrels *et al.*, Astrophys. J. **611**, 1005 (2004).
[16] G. R. Ricker *et al.*, in *Gamma-Ray Burst and Afterglow Astronomy 2001: A Workshop Celebrating the First Year of the HETE Mission*, edited by G. R. Ricker and R. K. Vanderspek, AIP Conf. Proc. 662 (AIP, New York, 2003), p. 3.
[17] C. Winkler *et al.*, Astron. Astrophys. **411**, L1 (2003).
[18] S. E. Woosley, Astrophys. J. **405**, 273 (1993).
[19] D. Eichler, M. Livio, T. Piran, and D. N. Schramm, Nature (London) **340**, 126 (1989).
[20] B. Paczyński, Acta Astronomica **41**, 257 (1991).
[21] J. Hjorth *et al.*, Nature (London) **423**, 847 (2003).
[22] S. E. Woosley, R. G. Eastman, and B. P. Schmidt, Astrophys. J. **516**, 788 (1999).
[23] N. Gehrels *et al.*, Nature (London) **437**, 851 (2005).
[24] J. S. Villasenor *et al.*, Nature (London) **437**, 855 (2005).
[25] D. B. Fox *et al.*, Nature (London) **437**, 845 (2005).
[26] J. Hjorth *et al.*, Nature (London) **437**, 859 (2005).
[27] C. L. Fryer, S. E. Woosley, and D. H. Hartmann, Astrophys. J. **526**, 152 (1999).
[28] N. Gehrels *et al.*, Nature (London) **444**, 1044 (2006).
[29] P. Jakobsson *et al.*, Mon. Not. R. Astron. Soc. **362**, 245 (2005).
[30] L. Christensen, J. Hjorth, and J. Gorosabel, Astron. Astrophys. **425**, 913 (2004).
[31] E. Berger *et al.*, Astrophys. J. **634**, 501 (2005).
[32] C. Conselice *et al.*, Astrophys. J. **633**, 29 (2005).
[33] D. Guetta and T. Piran, Astron. Astrophys. **435**, 421 (2005).
[34] E. Nakar, A. Gal-Yam, and D. B. Fox, Astrophys. J. **650**, 281 (2006).
[35] D. Guetta and T. Piran, Astron. Astrophys. **453**, 823 (2006).
[36] C. Ott, A. Burrows, E. Livne, and R. Walder, Astrophys. J. **600**, 834 (2004).
[37] H. Dimmelmeier, J. A. Font, and E. Müller, Astron. Astrophys. **393**, 523 (2002).
[38] È. È. Flanagan and S. A. Hughes, Phys. Rev. D **57**, 4535 (1998).
[39] U. Sperhake, B. Kelly, P. Laguna, K. L. Smith, and E. Schnetter, Phys. Rev. D **71**, 124042 (2005).
[40] J. G. Baker, J. Centrella, D. I. Choi, M. Koppitz, and J. van Meter, Phys. Rev. D **73**, 104002 (2006).
[41] L. Cadonati, Classical Quantum Gravity **21**, S1695 (2004).
[42] B. Abbott *et al.*, Phys. Rev. D **72**, 042002 (2005).
[43] B. Abbott *et al.*, Nucl. Instrum. Methods Phys. Res., Sect. A **517**, 154 (2004).
[44] K. Hurley, in *Encyclopedia of Astronomy and Astrophysics*, edited by P. Murdin (AIP, New York, 2002).
[45] R. Aptekar *et al.*, Space Sci. Rev. **71**, 265 (1995).
[46] http://gcn.gsfc.nasa.gov.
[47] http://space.mit.edu/HETE.
[48] M. J. Rees and P. Mészáros, Astrophys. J. **430**, L93 (1994).
[49] C. S. Kochanek and T. Piran, Astrophys. J. **417**, L17 (1993).
[50] T. Piran, Phys. Rep. **314**, 575 (1999).
[51] P. Mészáros, Rep. Prog. Phys. **69**, 2259 (2006).
[52] http://www.lsc-group.phys.uwm.edu/cgi-bin/cvs/viewcvs.cgi/matapps/src/searches/burst/multigrb/?cvsroot=lscsoft&sortby=rev#dirlist.
[53] L. S. Finn, S. D. Mohanty, and J. D. Romano, Phys. Rev. D **60**, 121101(R) (1999).
[54] P. Astone *et al.*, Phys. Rev. D **66**, 102002 (2002).
[55] P. Astone *et al.*, Phys. Rev. D **71**, 042001 (2005).
[56] C. W. Helstrom, *Statistical Theory of Signal Detection* (Pergamon Press, London, 1968), 2nd ed.
[57] S. Mohanty, Classical Quantum Gravity **22**, S1349 (2005).
[58] E. L. Lehman, *Nonparametrics* (Prentice Hall, Englewood Cliffs, NJ, 1998).
[59] K. S. Thorne, in *300 Years of Gravitation*, edited by S. W. Hawking and W. Israel (Cambridge University Press, Cambridge, England, 1987), pp. 330–457.
[60] K. Hagiwara *et al.* (Particle Data Group), Phys. Rev. D **66**, 010001 (2002).
[61] S. D. Mohanty, Classical Quantum Gravity **23**, S723 (2006).
[62] http://www.ligo.caltech.edu/~lazz/distribution/LSC_Data/.
[63] V. Bromm and A. Loeb, Astrophys. J. **575**, 111 (2002).
[64] Z. Bagolyi *et al.*, Astron. Astrophys. **453**, 797 (2006).
[65] R. A. Isaacson, Phys. Rev. **166**, 1272 (1968).
[66] A. S. Fruchter *et al.*, Nature (London) **441**, 463 (2006).
[67] C. L. Fryer, D. E. Holz, and S. A. Hughes, Astrophys. J. **565**, 430 (2002).
[68] http://swift.gsfc.nasa.gov.
[69] F. Dyson, in *Interstellar Communication*, edited by A. G. W. Cameron (Benjamin Press, New York, 1963).
[70] M. Shibata, M. D. Duez, Y. T. Liu, S. L. Shapiro, and B. C. Stephens, Phys. Rev. Lett. **96**, 031102 (2006).
[71] M. Shibata and K. Taniguchi, Phys. Rev. D **73**, 064027 (2006).
[72] B. Abbott *et al.*, Phys. Rev. D **72**, 082001 (2005).
[73] M. Shibata and K. Uryu, Prog. Theor. Phys. **107**, 265 (2002).
[74] R. Oechslin and H.-T. Janka, Phys. Rev. Lett. **99**, 121102 (2007).
[75] F. Loffler, L. Rezzolla, and M. Ansorg, Phys. Rev. D **74**, 104018 (2006).
[76] M. Shibata and K. Uryu, Phys. Rev. D **74**, 121503 (2006).
[77] J. A. Faber *et al.*, Astrophys. J. **641**, L93 (2006).
[78] S. Klimenko, S. Mohanty, M. Rakhmanov, and G. Mitselmakher, Phys. Rev. D **72**, 122002 (2005).
[79] M. Rakhmanov, Classical Quantum Gravity **23**, S673 (2006).
[80] S. D. Mohanty *et al.*, Classical Quantum Gravity **23**, 4799 (2006).
[81] M. H. van Putten *et al.*, Phys. Rev. D **69**, 044007 (2004).